

Measurement report: Violent biomass burning and volcanic eruptions: a new period of elevated stratospheric aerosol over Central Europe (2017 to 2023) in a long series of observations

5 Thomas Trickl¹, Hannes Vogelmann¹, Michael D. Fromm², Horst Jäger¹, Matthias Perfahl¹
and Wolfgang Steinbrecht³

¹Karlsruher Institut für Technologie, Institut für Meteorologie und Klimaforschung (IMK-IFU),
Kreuzeckbahnstr. 19, D-82467 Garmisch-Partenkirchen, Germany

²Naval Research Laboratory, 4555 Overlook Avenue, Washington, D.C., U.S.A.

10 ³Meteorologisches Observatorium, Deutscher Wetterdienst, Albin-Schwaiger-Weg 10, 82383 Hohenpeißenberg,
Germany

Correspondence to: Dr. Thomas Trickl, thomas@trickl.de, Tel. +49-8821-50283; Dr. Hannes Vogelmann,
hannes.vogelmann@kit.edu

15 **Abstract.** The highlight of the meanwhile 50 years of lidar-based aerosol profiling at Garmisch-Partenkirchen
has been the measurements of stratospheric aerosol since 1976. After a technical breakdown in 2016, they have
been continued with a new, much more powerful system in a vertical range up to almost 50 km a.s.l. that allowed
to observe very weak volcanic aerosol up to almost 40 km. The observations since 2017 are characterized by a
number of spectacular events, such as the Raikoke volcanic plume equalling in integrated backscatter coefficient
20 that of Mt. St. Helens in 1981 and severe smoke from several big fires in North America and Siberia with
backscatter coefficients up to the maximum values after the Pinatubo eruption. The smoke from the violent 2017
fires in British Columbia gradually reached more than 20 km a.s.l., unprecedented in our observations. The
sudden increase in frequency of such strong events is difficult to understand. Finally, the plume of the
spectacular underwater eruption on the Tonga islands in the southern Pacific in January 2022 was detected
between 20 and 25 km.

25 *Key words:* Lidar, system upgrade, stratospheric aerosol

1 Introduction

30 In view of its impact on the radiation budget and air chemistry the stratospheric aerosol layer has been monitored
since 1972 with balloon- and satellite-borne sensors as well as with lidar (Deshler 2006; 2008; Kremser et al.
2016; Vernier et al., 2016; Bingen et al., 2017; Thomason et al., 2018; 2021). Ground-based lidar with its good
vertical resolution became an important tool almost right from the beginning of long-term sounding (McCormick
et al., 1978; Simonich and Clemesha, 1997). A number of stratospheric aerosol sounding stations provided
routine long-term measurements at different latitudes (e.g., Osborn et al., 1995; Jäger, 2005; Deshler et al., 2006;
2008; Trickl et al., 2013; Khaykin et al., 2017; 2018; Zuev et al, 2017; 2019; Chouza et al., 2020) and since the
1990s in part adopted by the Network for the Detection of Stratospheric Change (NDSC, now: NDACC,
35 Network for the Detection of Atmospheric Composition Change).

The observations have yielded evidence of the mainly volcanic nature of the stratospheric aerosol. Long-lasting aerosol loading is only expected for a significant penetration of a volcanic plume into the stratosphere (Deshler, 2008). Secondary sources are strong injections from biomass burning (e.g., Fromm and Servranckx, 2003; Fromm et al., 2000; 2008a, b; 2010; 2019; 2022; de Laat et al., 2012; Khaykin et al., 2020; Lestrelin et al., 2021, 40 Ohneiser et al., 2022; Peterson et al., 2021), likely to be more important in a warmer climate, or emissions by air traffic. Also a potential influence of the growing Asian SO₂ emissions from coal burning has been discussed (Hofmann et al., 2009; Vernier et al., 2015). In addition, desert dust from Africa and Asia has been observed in the lower stratosphere (Trickl et al., 2013; Murphy et al., 2021).

The mid-latitude stratospheric aerosol level after a significant particle injection is subject to decay. Time series 45 yield a full decay time of about five years for tropical eruptions such as El Chichon (1982) and Pinatubo (1991), the 1/e decay time for the Pinatubo plume over Europe being 15 months (Ansmann et al., 1997). This is explained by an atmospheric updraft creating a tropical stratospheric reservoir layer. Poleward transport of aerosol from this reservoir in the Brewer-Dobson circulation (Treppe and Hitchman, 1992; Butchart et al., 2006; Butchart, 2014) leads to filling the mid-latitude losses by downward transport for many years. Aerosol removal 50 is also due to dilution (Fromm et al., 2008b) and, in the mid-latitudes, by processes like tropopause folding (Holton et al., 1995; Stohl et al., 2003). In fact, aerosol has been observed in stratospheric air intrusions into the troposphere after pronounced eruptions (e.g., Browell et al., 1987; Trickl et al., 2016). Total decay times for mid-latitude eruptions or fires are of the order of one year or less.

North American and Siberian fires can yield very strong contributions over Europe. Pronounced Canadian events 55 have been frequently observed in the troposphere (e.g., Forster et al., 2001; Müller et al., 2005; Petzold et al., 2007; Ancellet et al., 2016; Trickl et al., 2015; Markowicz et al., 2016). Also in the stratosphere, dense Canadian smoke plumes have been observed with growing occurrence (e.g., Fromm et al., 2010, 2020; 2022; and other papers cited above). The most spectacular event was that of the wild fires in British Columbia starting in August 2017. Peterson et al. (2018) and Fromm et al. (2021) report that the mass of smoke aerosol particles injected into 60 the lower stratosphere from five near-simultaneous intense pyro-cumulonimbus (pyroCb) events occurring in western North America on 12 August 2017 was comparable to that of a moderate volcanic eruption, and one order of magnitude larger than previous benchmarks for extreme pyroCb activity.

These plumes were registered and followed in time at many stations within EARLINET (Khaykin et al., 2018; Ansmann et al., 2018; Baars et al., 2019; EARLINET: European Aerosol Lidar Network, Bösenberg et al., 65 2003). As we will discuss in this paper (Sect. 3) the smoke gradually rose to more than 20 km above the Northern Alps. Ansmann et al. (2018) determined an extreme aerosol optical thickness (AOT) close to 1.0 at 532 nm in this layer that crossed central Europe at a height of 3 to 17 km on 21 to 22 August 2017. They concluded from measurements at three stations (Leipzig, Hohenpeißenberg (both Germany) and Kosetice (Czech Republic)) that the stratospheric light-extinction coefficients observed at a height of 14 to 16 km, were up to 70 twenty times higher than the maximum extinction coefficients reached after the Mt. Pinatubo eruption in June 1991 (Ansmann et al., 1997; Jäger, 2005).

This event was just the first of several strong fires that yielded significant aerosol loading of the stratosphere in recent years. In this paper, we discuss the related measurements in Garmisch-Partenkirchen (Germany). The period since 2017 has been one of the most interesting segments in the long-term stratospheric lidar sounding series that now

75 covers a total of 47 years (Jäger, 2005; Trickl et al., 2013). We first outline the history of the three lidar systems
so far used (Sect. 2.1) and describe the most important properties of the demanding data-evaluation procedure in
order to underline the quality of the data (Sect. 2.2). In Sect. 3.1 we present the Garmisch-Partenkirchen series of
the stratospheric integrated aerosol backscatter coefficient presented that extends from October 1976 to October
80 since 2017 with five aerosol peaks in the lower stratosphere from the 2017 fires in British Columbia, the
Raikoke volcanic eruption, the Colorado fires in autumn 2020, violent fires in British Columbia in 2021, and the
highly explosive Tonga eruption in 2022. The analysis benefits for the first time in our series from transport
modelling over almost two weeks combined with satellite data, as well as on information in the source region
and information available on the aerosol bursts themselves.

85 **2 Methods**

2.1 System history

The stratospheric lidar measurements were made until January 2016 with two lidar systems at IMK-IFU (until
2001 IFU, i.e., Institut für Atmosphärische Umweltforschung of the Fraunhofer Society; 47° 28' 37" N, 11° 3'
52" E, 730 m a.s.l.). In the following, lidar operation was resumed with a new system at the nearby high-altitude
90 station Schneefernerhaus (Umweltforschungsstation Schneefernerhaus, UFS, 47° 25' 00" N, 10° 58' 46" E, 2675
m a.s.l.) on the south side of Mt. Zugspitze (2962 m a.s.l.), about 9 km to the south-west of IMK-IFU.

Ruby lidar

The first system was delivered in 1973 by Impulsphysik G.m.b.H., based on a ruby laser, and, in addition to a
large number of routine and campaign-type tropospheric measurements (e.g., Reiter and Carnuth, 1975; Jäger et
95 al., 1988). After adding a photon-counting system the lidar was almost continually used for night-time
measurements of stratospheric aerosol since October 1976 (Reiter et al., 1979; Jäger, 2005).

Lidar container

After the ruby laser quit operation in 1990 the lidar was rebuilt in a container as a transportable, spatially
scanning system with a Nd:YAG laser (Quanta Ray, GCR 4, 10 Hz repetition rate, about 700 mJ per pulse at 532
100 nm), starting in 1991 for additional investigation of contrails (Freudenthaler, 2000; Freudenthaler et al., 1994;
1995). The 0.52-m Cassegrain receiver of the 1973 system was retained. The laser was delivered early enough to
resume the measurements just before the Pinatubo eruption. The lidar was used for both free-tropospheric (e.g.,
Jäger et al., 2006; Forster et al., 2001; Trickl et al., 2003; 2011) and stratospheric (Jäger, 2005) measurements.
The vertical bins of this 300-MHz multichannel scaler (FAST ComTec) were set to 75 m. Four subsequent
105 measurements were made without attenuation and with three different attenuators, the strongest one being used
for the near-field detection. A high-speed chopper was set to cut off the strongest part of the signal. For each
attenuation step a different chopper delay was applied (minimum distance achieved: 1.3 km).

This second lidar system contributed to both NDACC (Network for the Detection of Atmospheric Composition
Change; www) and EARLINET. The data in the data bases are not smoothed which in the case of strong

110 extinction leads to noise spikes in the lowest data segments up to the tropopause region where the photon-
counting signals were attenuated for minimizing counting dead-time (pulse-overlap) effects. With this lidar
system rather small aerosol structures exceeding roughly 2 % of the Rayleigh return at 532 nm (that corresponds
to a visual range of more than 400 km above 3 km) could be resolved within the free troposphere and lower
stratosphere. The aerosol backscatter coefficients could be calculated with a relative uncertainty of 10 to 20 %
115 under optimum conditions.

This lidar container was used to extend the stratospheric aerosol series (Jäger, 2005; Trickl et al., 2013) until
2016. The end was caused by a degradation of the container and components, however eventually fatal problems
in the data transfer from the counting system to the computer after a measurement. These problems are reflected
by the diminishing number of stored data in 2014 and 2015 and led to abandoning the system in early 2016.

120 *UFS lidar (2675 m a.s.l.)*

The new lidar at UFS is integrated into the water-vapour differential-absorption lidar (DIAL; Vogelmann and
Trickl, 2008) by sharing its 0.65-m-diameter Newtonian receiver (providing a 56-% gain in area) and its
polychromator box. On 29 September 2017 a Spitlight DPSS frequency-doubled injection-seeded Nd:YAG laser
from Innolas (wavelength 532.24 ± 0.02 nm) replaced the pump laser of the DIAL. Thus, the repetition rate
125 could be increased from 20 Hz to 100 Hz, the second-harmonic pulse energy being 140 mJ instead of 200 mJ.
The number of laser shots in a single measurement was gradually increased to 100000 (16.7 min; Table 1).

The operation of the system at this elevated site offers the benefit of much clearer average conditions because it
is frequently located outside the Alpine boundary layer (e.g., Carnuth and Trickl, 2000; Carnuth et al., 2002),
including cloud-free conditions during night-time. In addition, despite shortening the distance to the stratosphere
130 by just 1945 m a considerable gain in signal is obtained. This is explained by the extreme near-field drop of the
backscatter signal with the distance and the requirement to select the same setting of the maximum detector
output voltage at both locations (typically 70 mV into 50Ω for the detector type used, see below). A simulation
shows that even at 25 km a.s.l. the gain in signal is still a factor of 1.5. This factor, together with the larger
receiver, helps to avoid a lot of expensive additional laser photons.

135 The polychromator of the DIAL is used as described by Vogelmann and Trickl (2008). Near-field and far-field
signals are separated by a beam splitter. The far-field channel contains a blade placed in a focal point that cuts
off the near-field return. Residual background radiation (e.g., scattered light from local sources) is strongly
reduced by an interference filter with 0.5 nm full width at half maximum (Barr Associates). In the near-field
channel the very strong return is attenuated by two decades by a neutral-density filter (Andover).

140 The electronics used share the highly linear approach of the lidar systems of IMK-IFU (Trickl et al., 2020a;
2023; Klanner et al., 2021). The high linearity of the data is ensured by Hamamatsu R7400U-03 photomultiplier
tubes (with actively stabilized socket and a high-speed discriminator junction from Romanski Sensors, RSV),
Licel transient digitizers (12 bits, 20 MHz, equipped with ground-free input) and a FastComtec MCS6A 5-GHz
photon-counting system. The data are processed at 7.5-m height intervals.

145 One great advantage of the new data acquisition is that it is no longer exclusively based on single-photon
counting as until 2015 which had required strong attenuation of the signals in the case of near-field detection in
order to avoid the photon-pulse overlap issues. Without attenuation the relative contribution of the near-field

noise is greatly reduced. The analogue signal for the near-field and far-field detectors is fully linear up to distances r of more than 15 km and more than 30 km, respectively (after a tiny exponential correction, Trickl et al., 2020a). Due to the narrow spectral filtering the noise from the solar background is sufficiently reduced to allow daytime measurements with the analogue channels up to 30 km. The best performance of the analogue channels is achieved if the peak signal is kept below 70 mV.

The photon-counting data are useful without smoothing to more than 50 km a.s.l. The PMT tests over one hour (Klanner et al., 2021) have demonstrated the absence of dark counts (thermal emission from the photocathode). The night-time lidar background is not fully zero (about 50 counts) which may be improved.

Another great advantage of this system over the old ones is that it can be operated under remote control, in particular benefitting from the corresponding features of the new laser. During a field campaign in the United States in summer 2018 the routine measurements at UFS were started from the other side of the Atlantic Ocean.

We also plan to add a 355-nm channel, a depolarization channel as well as a 532-nm high-spectral-resolution channel for extinction measurements during periods of strong stratospheric aerosol loading, as a contribution to the European ACTRIS (Aerosol, Clouds and Trace Gases Research Infrastructure) network.

2.2 Data evaluation

The quality of stratospheric aerosol backscatter coefficients critically depends on the procedures applied. Because of the ongoing discussions within NDACC we outline in the following the most important properties of the approach chosen. The careful procedure, just very briefly sketched by Jäger (2005), has been refined, motivated by the improved signal-to-noise ratio of the new system.

For the measurements until 2011 (Jäger, 2005; Trickl et al., 2013) an iterative approach for calculating the aerosol backscatter coefficients was chosen. Afterwards, an extended-Klett (Klett, 1985) program has been used that was originally developed and very successfully quality assured for aerosol retrievals within EARLINET.

The sign error in Eq. 20 of Klett (1985) is corrected, yielding Eq. 2 of Eisele and Trickl (2005; see also Speidel and Vogelmann, 2023). The Klett downward inversion typically starts at a distance of 45 km (47.675 km a.s.l.). This program uses an approach for the extinction-to-backscatter ratio (lidar ratio) with up to ten layers. Since 2012, a lidar ratio of 50 sr has been applied in the troposphere, 45 sr in the stratosphere. The latter value is valid approximately within ± 7 sr for periods outside the extreme eruptions of El Chichon and Pinatubo (Jäger and

Deshler, 2003). Because of the mostly low extinction of stratospheric aerosol the choice of the lidar ratio is normally not critical. In the presence of cirrus clouds or particularly strong aerosol peaks at least one additional layer is introduced whenever a calibration of the aerosol backscatter coefficients is possible below the clouds (Eisele and Trickl, 2005). In cirrus layers typical values of the lidar ratio of 10 sr to 30 sr are retrieved, the higher values most likely corresponding to cases of non-persistent clouds during the measurement period.

A key issue of the retrieval is an accurate calculation of the Rayleigh backscatter coefficients (see Appendix). This requires the calculation of the atmospheric air density from sufficiently accurate meteorological data. The molecular return is simulated by calculating the atmospheric density from the routine radiosonde ascents at Oberschleißheim ("Munich" radiosonde, station number 10868, 101 km roughly to the north; <http://weather.uwyo.edu/upperair/sounding.html>) and, above the maximum altitude of the sondes, by using NCEP (National Centers for Environmental Prediction) meteorological data up to more than 50 km, daily

interpolated for our station for 12 UTC (13 CET; meanwhile available at: <https://www-air.larc.nasa.gov/misions/ndacc/data.html#>). All sonde and NCEP altitudes are converted from geopotential to absolute units.

The new approach accounts for Raman scattering (see Appendix). In the near-field channel the complete Raman band is detected. The interference filter in the far-field channel cuts off most of the S- and O-branch
190 contributions of oxygen and nitrogen.

As an example for the high data quality we show in Figure 1 the results of the retrieval for a measurement on 7 January 2021 between 18:18 and 18:35 CET (Central European Time = UTC + 1 h). The Klett solutions for the three detection channels are displayed. The agreement of the curves in regions of overlap is excellent, after very small exponential corrections of the analogue signals (Sect. 2.1) that are optimized by comparison with the
195 photon-counting signal in aerosol-free altitude ranges. At large distances r the noise of the values from the photon-counting data is significantly lower than that of the analogue data and no artificial structure is seen. The counting noise level in the raw data decreases with altitude. Due to the multiplication of the signals with r^2 during the Klett inversion an almost constant noise level is reached.

The calibration of the backscatter coefficients is additionally controlled by the requirement that the backscatter
200 coefficients must stay positive. Here, it is beneficial that layers without aerosol quite frequently occur in the upper troposphere.

The raw backscatter signals have been corrected for the light absorption by ozone in the stratosphere cross section for both the ruby wavelength (before 1990) and the wavelength of the frequency-doubled Nd:YAG laser (Brion et al., 1998; http://igaco-o3.fmi.fi/ACSO/cross_sections.html). The values for $\lambda_{\text{air}} = 532.092$ nm are
205 almost temperature independent, ranging between $2.812 \times 10^{-25} \text{ m}^2$ (295 K) and $2.805 \times 10^{-25} \text{ m}^2$ (218 K). Climatological, seasonally varying ozone profiles have been taken, kindly provided by the nearby Meteorological Observatory Hohenpeißenberg of the German Weather Service (MOHp). Figure 2 shows that these corrections are by no means negligible in the altitude range of maximum ozone concentrations.

An accurate determination of the tropopause altitude is crucial for the accurate calculation of the integrated
210 backscatter coefficient in the stratosphere. It is normally extracted from the temperature data from the Munich radiosonde. Both the values for the WMO criterion (WMO, 1986) and the temperature minimum are calculated. These values have been compared since 2012 with a number of ancillary data and modified if necessary (in rare cases). The validation and modification is derived from the ozone rise provided by the ozone differential-absorption lidar at IMK-IFU (Trickl et al., 2020a) whenever available, the drop of relative humidity in the sonde
215 data and the upper edge of cirrus clouds (if present). Also the aerosol distribution in the tropopause region (e.g., cirrus clouds) has been used for refinements in unclear situations.

Because of the strong drop in signal the near-field raw data were smoothed with a linearly growing interval, using the Blackman-type numerical filter of Trickl et al. (2020a). At $r = 10$ km the interval size reaches ± 13 bins (± 100 m), corresponding to a vertical resolution of roughly 40 m in the VDI definition and roughly 70 m as
220 defined by the full width at half maximum of the response to a delta function (Trickl et al., 2020a).

A discussion of the uncertainties is given in the Appendix.

3 Results

225 3.1 Series of the integrated backscatter coefficient (1976 – 2023)

Figure 3 shows the updated version of the time series of the stratospheric integrated backscatter coefficient from 26 October 1976 to 11 October 2023. The integration starts at 1 km above the tropopause in order to reduce the influence of contributions of mixed tropospheric and stratospheric character. Since we cannot easily repeat the evaluation of the old data with all the microphysical details we continued our tradition and converted the values
230 from 532.24 nm to the ruby-laser wavelength of 694.3 nm (Jäger and Deshler, 2002; 2003).

In 2014 and 2015 the number of the measurements that could be stored in the computer strongly diminished due to data transfer issues, and the old lidar system was abandoned after a final measurement on 29 January 2016. Typical scattering ratios were about 1.05, i.e., rather low, but higher than the very small pre-2006 background.

235 With the new system the routine sounding was resumed in 2017, after one test measurement on 17 March 2016. Until the end of the series several pronounced peaks are seen. The decay in 2022 led to values next to the 1979 level, before a new phase of elevated aerosol prevented a return to a more pronounced background phase. In Table 1 we list some of the conditions of the measurements since 2017.

There is an obvious winter-summer modulation, visible in particular during the low-background period. This is mostly due to the changing tropopause. For example, the peak in January 2019 is mainly caused by tropopause
240 altitudes of about 10 km, whereas they were of the order of 12 km in February. The seasonal cycle is somewhat obscured by occasional plumes just above the tropopause.

Between early 2014 and August 2017 there were just three major eruptions, all in the tropics (<https://volcano.si.edu/>; Massie, 2016; more information on individual cases: <https://volcano.si.edu/index.cfm>) and, thus, not so important for observations at our latitude, but can contribute to the background with a delay of
245 the order of half a year (Jäger, 2005). The Kelut plume (Java, volcanic explosivity index (Newhall and Self, 1982) VEI = 4) reached as much as 17 km on 13 February 2014, and Manam (New Guinea) 19.8 km in a possibly brief explosion on 31 July 2015. The eruption of Cotopaxi is special since this volcano in Equador is the highest active volcano on this planet (5897 m). The material reached 17.9 km a.s.l. on 15 August 2015, not far from the tropical tropopause.

250 Between 2017 and February 2023 three eruptions may have influenced our series. In 2019 the volcanoes Raikoke (Kuril Islands) and Ulawun (New Guinea) spewed material into the stratosphere. On 15 January 2022 a particularly explosive eruption was reported on the Tonga islands that reached about 58 km (Proud et al., 2022; Taha et al., 2022). Due to its occurrence in the southern hemisphere related particles were detected above Garmisch-Partenkirchen not before October, except for a single, accidental observation on 29 June 2022.

255 The pronounced peaks of the integrated backscatter coefficient registered with the new system since 2017 will be discussed in the following. Most importantly, in addition to the volcanic eruptions, a number of exceptionally violent fires led to significant rises in stratospheric aerosol. These fire events make this period particularly interesting, with peak backscatter coefficients and peak altitudes unprecedented for smoke in our series. In contrast to earlier years a much better analysis of the sources of stratospheric aerosol has become possible by a
260 combination of extended transport modelling and satellite data.

3.2 Sudden increase of the occurrence of fire plumes deeply penetrating into the stratosphere

Until July 2017 volcanic eruptions were the main source of stratospheric aerosol detected above our site. An exception was the remarkable aerosol loading following a fire in Québec in June 1991 just before the arrival of the Pinatubo plume (Fig. 3) that reached roughly 17 km above Garmisch-Partenkirchen (Carnuth et al., 2002; Fromm et al., 2010). After the big Chisholm fire in 2001 the IFU lidar detected aerosol to more than 6 km above the tropopause (Fromm et al., 2008, Fig. 3) for a short period of time. However, in the measurements in recent years penetration into the stratosphere to more than 20 km has been observed (Baars et al., 2019; Torres et al., 2020).

Although an increase in the occurrence of strong fires might be expected in a drier climate (Fig. 2 of Trickl et al., 2013) the sudden rise in the number of cases and their outstanding violence is rather surprising.

British Columbia fires 2017

The first, particularly spectacular signature after resuming the measurements at UFS in 2017 was identified as the result of the pyroCbs in British Columbia (B.C.) on 11 and 12 August 2017 that acted like a volcanic eruption (Peterson et al., 2018; Fromm et al., 2021). In general, the B.C. fire season during that year lasted several months, starting on 6 July. The tropospheric smoke plumes were repeatedly detected with the 313-nm channel of our ozone DIAL.

Our first observation of the B.C. plume with the UFS aerosol lidar took place on 25 August (Fig. 4), after a 17-day period without measurements. The daytime measurements (8 CET to 12 CET) with analogue data acquisition, apart from a few smaller peaks, showed a giant aerosol spike as high as 16 to 17 km a.s.l. The 532-nm backscatter coefficients ranged between $1.3 \times 10^{-6} \text{ m}^{-1} \text{ sr}^{-1}$ and $1.9 \times 10^{-6} \text{ m}^{-1} \text{ sr}^{-1}$, corresponding to scattering ratios (ratio $\beta_R + \beta_P / \beta_R$ of the backscatter coefficients) between 7.2 and 10.3. This value is exceptionally high for the stratosphere. For comparison, the Pinatubo maximum scattering ratio above our site in early 1992 was about 10 at 21 km. As mentioned in the introduction, even higher stratospheric aerosol loading caused by the B.C. fires was reported by Ansmann et al. (2018) farther to the north, a few days earlier.

The first burst of pyroCbs was reported by Fromm et al. (2021) for 12 August, at about 23:00 UTC, the last one at about 6:45 UTC on the following day. Several times altitudes between 13 km and 13.7 km were recorded by the Prince George radar.

Forward simulations with the HYSPLIT model (https://www.ready.noaa.gov/HYSPLIT_traj.php; Draxler and Hess, 1998; Stein et al., 2015) initialized over the pyroCb area at that time showed passage above the Bavarian Alps on 20 and 22 August, in agreement with the observations by Ansmann et al. (2018) carried out before our first available measurement day (25 August, see Fig. 4). The forward trajectories do not show the rise to more than 16 km that is documented in Fig. 4. One cannot exclude a thermally induced rise (de Laat et al., 2012; Khaykin et al., 2018; Torres et al., 2020; Lestrelin et al., 2021; Ohneiser et al., 2023). The rise of the plume was verified by the “curtains” of the space lidar CALIOP (Cloud-Aerosol Lidar with Orthogonal Polarization; https://www-calipso.larc.nasa.gov/products/lidar/browse_images/products/). Fromm et al. (2021) shows a rise from 13 km over the Canadian western arctic sea to more than 15 km over the northern part of the Hudson Bay. Lestrelin et

al. (2021) followed the CALIOP images to Europe and found splitting of the plume into three parts and a rise to higher altitudes.

300 An approximate source receptor relationship for 25 August was established by 315-h HYSPLIT ensemble backward trajectories (reanalysis mode), run for start altitudes above Garmisch-Partenkirchen between 15300 m and 17200 m a.s.l. at intervals 50 m. In this altitude range two principal branches are seen, one showing air passing over the United States (southern branch, SB), one reaching arctic Canada (northern branch, NB). Below 15850 m the SB is almost exclusive. Above this altitude the NB becomes increasingly important.

305 In numerous transport studies (e.g., Trickl et al., 2013; 2015; 2020b) during the past decade we found that the HYSPLIT trajectories explain our observations better in the reanalysis mode (using National Center for Environmental Prediction Reanalysis data). In this case and a case presented further below, the GDAS (Global Data Assimilation System) mode performs significantly better. In Fig. 5 we show the GDAS result for the altitude of 16860 m which yields the best proximity to the source region. The NB trajectories pass over the
310 Arctic regions where the plume was located with the CALIOP images and almost perfectly hit the pyroCb source region within less than half a day of the most active period, on 12 August after 12 UTC. Given the uncertainty of trajectory calculations, the considerable spreading of the trajectories towards the west and the complex meteorology associated with the pyroCbs (Lestrelin et al., 2021) this result is highly satisfactory. Most importantly, we do not know about any other similarly strong aerosol source for that period.

315 Fromm et al. (2021) show in their Figs. 3 and 9 the propagation of the densest part of the smoke close to the western end of the Great Slave Lake. In Fig 5, the trajectories pass this area farther to the west where less aerosol is depicted in that figure. This could explain why our peak backscatter coefficient is lower than that published by Ansmann et al. (2018). The backward trajectories slightly descend towards the source region, not enough to exclude a thermal rise of the plume.

320 Between 25 August 2017 and the end of the year a total of 30 measurements were conducted. For the series image in Fig. 3 just one measurement per day was selected. Frequently daytime measurements took place. Until spring 2018 just analogue data acquisition was available that is fortunately highly linear after just minor correction (Sect. 2, Table 1).

On the following measurement day, 29 August (not shown), the big feature at 16.5 km from the first passage
325 over Central Europe had disappeared. In October another maximum of the integrated backscatter coefficients was reached, tentatively ascribed to a more dispersed phase of the plume with a higher probability to pass over Southern Germany. The plume decayed considerably until December 2017 (for two autumn examples see Fig. 4). The layer top rose from 17 km (25 August 2017) to more than 24 km in February 2018. This is slightly above the highest altitudes reported by Baars et al. (2019) in an overview for the EARLINET stations. The spiky
330 structure of the backscatter profile gradually became smoother and disappeared in winter 2018 (not shown). The short decay of less than one year is typical of mid-latitude aerosol plumes in the stratosphere, as can be concluded from Fig. 3 (e.g., St. Helens, 1980).

Apart from spreading to other latitudes stratospheric aerosol can be diminished by removal from the lowermost stratosphere in tropopause folds (e.g., Browell et al., 1987; Trickl et al., 2016). Also in autumn 2017 aerosol was
335 found in stratospheric intrusion layers in our ozone soundings in the valley at IMK-IFU, this time during a period of aerosol from biomass instead of a volcanic plume in the lower stratosphere. Figure 6 shows three ozone

and 313-nm-aerosol profiles obtained with our ozone DIAL (Trickl et al., 2020a) in the morning of 2 October 2017, before the arrival of clouds (see aerosol spike at 9.45 km) around noon stopped the measurements. The descending intrusion layer, originating at more than 10 km over Northern Canada three to four days earlier, is characterized by ozone mixing ratios up to almost 140 ppb, in agreement with the morning balloon-borne measurement at Hohenpeißenberg, 38 km to the north from UFS (Trickl et al., 2023). The minimum Hohenpeißenberg sonde RH is constantly 2 %, most likely a wet bias (Trickl et al., 2014; 2016). The aerosol backscatter coefficient in this layer reached $2 \times 10^{-7} \text{ sr}^{-1} \text{ m}^{-1}$ which is moderate in comparison with other cases, in particular the record-setting $2.35 \times 10^{-6} \text{ m}^{-1} \text{ sr}^{-1}$, observed on 7 September 2009 after the violent eruption of Sarychev (Trickl et al., 2020b). It is interesting to see that the elevated aerosol backscatter coefficients do not fill the entire intrusion layer although the width scales similarly as that of elevated ozone. In the case described by Trickl et al. (2016) the aerosol maximized in the upper part of the intrusion.

Siberian fires 2019

Parallel to violent volcanic eruptions (Sect. 3.3) extreme and long-lasting wildfires in central and eastern Siberia were reported in the summer of 2019 (Johnson et al., 2021). Ohneiser et al. (2021) describe an Arctic field campaign in September and October 2019 with an advanced multi-wavelength polarization Raman lidar onboard the German icebreaker Polarstern. The high lidar ratio indicated that the stratospheric aerosol observed at high latitudes was smoke. The air mass could be traced back to fires in Siberia. Also over Central Europe they report for Leipzig and other lidar stations a contribution of these fires (see also Ansmann et al., 2021). In the absence of strong pyro-convection they conclude that the biomass-burning particles were limited to altitudes up to 13 km. It is difficult for us without the planned high-spectral-resolution detection channel to distinguish between the volcanic aerosol and the Siberian smoke. For more information on this period see Sect. 3.3.

Colorado fires 2020

The measurements in November and December 2020 were characterised by numerous spikes in the backscatter profiles in the upper troposphere and lower stratosphere (Fig. 7; the number of profiles is too low for a contour plot). The rather narrow structures on a broad background indicate sources just shortly backward in time. We ascribe these narrow aerosol layers to very late fires in Colorado. The narrow features harden the idea of rather fresh emissions. Indeed, HYSPLIT ensemble backward trajectories show an air-mass passage over that region. According to the MODIS (Moderate Resolution Imaging Spectroradiometer on board NASA's Aqua satellite) web site the 2020 Colorado fire season has been devastating and record-breaking. The three largest fires in Colorado history all occurred during this year (https://modis.gsfc.nasa.gov/gallery/individual.php?db_date=2020-10-27). The two most violent fires occurred in October 2020, very late in the year. The Cameron Peak Fire burned 844 km² and the East Troublesome Fire burned 779 km². The Cameron Peak Fire began in August and is the largest fire in state history, the nearby East Troublesome pyroCb ignited on October 14 and explosively grew until 21 October (13.2 km) to capture the number-two title. At least 11 fires continued to be active in the state on October 26.

The plume was traceable around the world with satellite-based instruments such as MODIS, CALIOP, and vertical soundings of the Micropulse Lidar Network (MPLNET, <https://mplnet.gsfc.nasa.gov/>). The particles from the East Troublesome October 21 pyroCb in Colorado can be seen to flow over the Atlantic Ocean to reach Europe and North Africa on 25 October. Our first lidar measurement after the occurrence of the pyroCb on 28 October (not shown) shows small aerosol peaks above the smooth background between the tropopause and 14 km that could be a first indication of the fire plume. HYSPLIT ensemble backward trajectories initiated in this altitude range show zonal flow from Colorado to the Alps within just three days. The measurements during the following weeks (Fig. 7) show strongly varying structures and were not analysed in detail because of this complexity except for 9 November. The source-receptor relationship for the lidar measurements UFS on 9 November was hardened by the satellite and MPLNET measurements mentioned above, connected via HYSPLIT forward and backward trajectories. HYSPLIT ensemble trajectories initiated at and around 14.5 km a.s.l. above UFS on 9 November show a rather coherent near-zonal flow around the globe passing over North America twice within 315 h.

While the East Troublesome pyroCb is a plausible source for these November stratospheric layers, we cannot rule out contributions from earlier pyroCbs in the USA. For instance, the Creek fire in California developed its own spectacular pyroCb on 3 September, injecting smoke upward of 16 km (Hu et al., 2022; Lareau et al., 2022). Late Californian contributions (26 October to 3 November) were found in the upper troposphere above the Mediterranean region (Michailidis et al., 2023; Mamouri et al., 2023).

390 *Spectacular pyro-cumulonimbus in British Columbia on 30 June 2021*

The measurements on 11 and 21 July 2021 show pronounced stratospheric aerosol signatures that lead to clearly enhanced backscatter coefficients (Fig. 3). We discuss here just the particularly spectacular case of 11 July (Fig. 8). We observed enhanced aerosol structure in the upper troposphere and in the stratosphere up to about 19.5 km. This upper edge is absent in earlier measurements during this season. There are four pronounced spikes between 13 and 16 km. The big spike at 15.6 km with a remarkable backscatter coefficient of $7.07 \times 10^{-7} \text{ m}^{-1} \text{ sr}^{-1}$ is very thin which indicates an event just a few days backward in time. The maximum value is more than half that obtained for the 2017 fires (see above). The 532.2 nm integrated backscatter coefficient rose to $6.59 \times 10^{-4} \text{ sr}^{-1}$ ($3.16 \times 10^{-4} \text{ sr}^{-1}$ at 694.3 nm, Fig. 3).

We relate this observation to high pyroCb activity on 30 June, again in British Columbia. There are reports on record-setting temperatures of more than 45° C in that region, a drought, numerous lightning strokes under dry conditions and huge fires. An article of the Washington Post of 1 July 2021 (<https://washingtonpost.com/weather/2021/07/01/wildfires-british-columbia-lytton-heat/>) gives a good overview, citing several scientists, and includes a picture with an impressive very thick smoke “mushroom” clearly reaching into the stratosphere. The pyro-Cb burst most likely responsible for our observation occurred at 51.0° N and 120.8° W, at times between 19 UTC on 30 June and after UTC midnight. The Seattle radar yields a maximum altitude of 17.3 km at 2:12 UTC. This altitude exceeds that of the largest peak in Fig. 7.

Unfortunately, we could not find a suitable “aerosol curtain” in the images derived from the measurements of CALIOP visualizing the fire plume right after the event. However, we inspected numerous graphics of the Multi-

angle Imaging SpectroRadiometer (MISR, <https://misr.jpl.nasa.gov/>) and the Micro-Pulse Lidar Network
410 (<https://mplnet.gsfc.nasa.gov/>) to establish the path of the smoke.

The interpretation was hardened by running numerous HYSPLIT 315-h forward and backward trajectories for different start altitudes with the GDAS option. As in the case of the 2017 fires there is no homogeneous flow pattern, the path of the trajectories strongly varying with altitude. In Fig. 9 we show ensemble trajectories initiated at 15.6 km a.s.l. and 23 UTC (24 CET) above IMK-IFU, the position of the largest aerosol spike in Fig.
415 8 and start positions varied by one grid point. As mentioned there is a strong sensitivity on start time and position. One trajectory bundle leads backward towards British Columbia and three trajectories from this bundle end not far from the position of the main pyro-Cb 261 h backward in time (1 July, 2 UTC, almost within the pyroCb period mentioned above). The trajectory results for the aerosol peaks between 12.3 km and 13.8 km are less perfect. Again, this result is highly satisfactory given the complex meteorology of a pyroCb including
420 radiation-induced lofting (see 2017 case).

The trajectory results provide evidence that the main burst of the plume directly passed over our site during the first round around the globe. This explains the very sharp structure of the spikes.

3.3 Volcanic eruptions in June 2019 then January 2022

Eruptions in 2019

425 In June 2019 there is the interesting case of an almost co-incident volcanic eruption in the tropics and in the mid-latitudes. According to information from the Global Volcanism Program (GVP) of the Smithsonian Institution (<https://volcano.si.edu/index.cfm>) the Raikoke volcano on the Kuril Islands (48.292° N and 153.23° E, summit 558 m a.s.l.) erupted on 21 June 2019. Cameron et al. (2020) reported strong SO₂ after Raikoke eruption at 24 km, tapering off within four months. Boone et al. (2022) and Knepp et al. (2022) discuss the satellite
430 observations of SO₂ and sulfate, the latter having been observable until the following spring, obviously at a different cut-off level.

Subsequently, Ulawun (New Guinea, 5.05° S and 151.33° E, summit 2334 m a.s.l.) violently erupted on 26 June 2019. The maximum altitude reached was 19.2 km which should be within the tropical stratosphere. A plume component at 16.8 km is reported to having drifted north-east- to north-westward. Both eruptions were studied
435 by Kloss et al. (2021).

Our first observation of two small aerosol peaks just above the tropopause that could be related to the Raikoke plume took place on 19 July 2019. The signal could not be inverted because tropospheric clouds strongly attenuated the signal. From 23 July to September first a number of spikes appeared between the tropopause and 19.5 km, i.e., less than the maximum plume height reported by Cameron et al. (2020). The spiky distribution
440 gradually changed to a less structured hump (Fig. 10). The maximum backscatter coefficient above the respective tropopause was $4.18 \times 10^{-7} \text{ m}^{-1} \text{ sr}^{-1}$ on 23 July (the unidentified spike at 12.8 km with $7.53 \times 10^{-7} \text{ m}^{-1} \text{ sr}^{-1}$ could be due to a cirrus). This is quite high for stratospheric aerosol. The maximum integrated backscatter coefficient was calculated for 22 August ($5.4 \times 10^{-4} \text{ m}^{-1} \text{ sr}^{-1}$, 693.4 nm). It exceeded those for the eruptions of
445 Mt. St. Helens and Alaid in the early 1980s and is the third highest in our series, following the maxima for Pinatubo and El Chichon. The temporary minimum of the integrated backscatter coefficient in September 2019

is caused by very high tropopause levels up to 15 km. The structured contributions after the Raikoke eruption gradually tapered off until January 2020, reaching a maximum altitude of 22 km. They were followed by a smooth hump with elevated aerosol (up to $5 \times 10^{-8} \text{ m}^{-1} \text{ sr}^{-1}$) ending between 20 and 21 km.

450 As mentioned in Sect. 3.2 Ansmann et al. (2021) and Ohneiser et al. (2021) emphasize the additional influence of Siberian fires during that summer. We defer to the view in that paper, derived from differences in the retrieved extinction-to-backscatter ratios. Ohneiser et al. (2021) conclude that the volcanic portion of the aerosol is mostly that at higher altitudes.

455 It is interesting that the decay of the integrated stratospheric backscatter coefficient is slower than after most mid- and higher-latitude volcanic eruptions (Fig. 3). We speculate that this could be due to the larger area of these strong fires in comparison with a volcanic point source and longer-lasting burning, leading to wider horizontal spread of the particles. Alternatively, Khaykin et al. (2022a) describe a long-lasting anticyclone that circumnavigated the globe three times, and ascended diabatically to 27 km altitude through radiative heating of volcanic ash in the plume.

460 There is some indication that we are able to distinguish between contributions from both 2019 eruptions in our data. This distinction is based on a delayed arrival of what we could ascribe to the tropical component (see (Jäger, 2005) for the eruptions of El Chichon and Pinatubo). On 20 December 2019 a sudden rise of the upper boundary of the stratospheric aerosol to clearly beyond 30 km started. Such a rise would require a Brewer-Dobson-type lifting of the tropical air mass.

465 In Fig. 11 we give a few examples of smoothed scattering ratios from the times before, during and after that period of enhanced aerosol. Up to 35 km the uncertainty of these values stays within ± 0.03 . The noise level above 35 km becomes rather high (up to ± 0.1) because the scattering ratio implies a division by the strongly decreasing molecular backscatter coefficient. It is, therefore, difficult to determine precisely the cut-off altitude if it lies between 35 and 40 km. The scattering ratio was almost constant up to the upper boundary and typically ranged between 1.04 and 1.10. This indicates a rather homogeneous aerosol distribution in agreement with the
470 idea of long transport times.

Figure 12 shows the time series of the principal aerosol upper boundaries determined from the retrieved profiles of the backscatter coefficients. The boundaries are crude estimates and (if discernible) correspond to altitudes where the aerosol disappears or reaches a bottom line. On 26 April 2021 the layer extension to beyond 30 km completely disappeared (Fig. 13). Apart from occasional very small peaks this remained unchanged until the end
475 of the measurements included in this paper.

These observations are further discussed in Sect. 4, in comparison with the Pinatubo results (Jäger, 2005).

Hunga Tonga 2022

480 The most violent volcanic eruption in recent history occurred on 15 January 2022, lasting just 11 h. The Hunga Tonga Hunga Ha'apai submarine volcano (20.55° S , 175.4° W) injected material, including huge amounts of steam (Schoeberl et al., 2022, Xu et al., 2022; Vömel et al., 2022), into the stratosphere up to as high as 58 km, far beyond the 40 km reached by the Pinatubo eruption (Proud et al., 2022; Taha et al., 2022). The bulk of the plume circulated the globe in the southern hemisphere at altitudes between 20 and 30 km. Most of the poleward expansion occurred in the southern hemisphere. However, some material also reached the Arctic. In the tropics

485 maxima between 20 and 45 ppm of water vapor were detected between 25 and 26 km by sonde ascents (Vömel et al., 2022).

But also at high latitudes observations of the plume were made. Taha (2022) traced an aerosol layer observed at 83° N, 29° E and 21 km on 4 April 2022 back to the Hunga Tonga cloud. Khaykin et al. (2022b) verified northward transport to 80° N within three to four months by using satellite and lidar measurements. The altitude range was 20 to 25 km (see also (Mishra et al., 2022)).

490 The only of our measurements showing a conspicuous feature in spring and summer 2022 was made on 29 June (Fig. 14). A small aerosol peak, not seen in other measurements during that period occurred at 22.75 km. This is between the altitudes in the observations of the Tonga plume at Haute Provence (Southern France) and Kühlungsborn (North Germany) as presented by Khaykin et al. (2022b).

In order to identify the advection path for the peak in Fig. 14 we calculated HYSPLIT 315-h backward
495 trajectories for re-analysis data and in ensemble mode (Fig. 15). The air mass arrived from the east and passed over China on 17 June. Figure 16 shows aerosol curtains of the Ozone Mapping and Profiler Suite (OMPS) limb sounder for the start and end times of the trajectories. On 29 June the orbits closest to Garmisch-Partenkirchen (UFS) a feature with elevated aerosol extinction ratio around 22.5 km conforms to the lidar observation. This is just indicative of the presence of Tonga particles. However, the Asian orbit on 17 June (lower panel) reveals a
500 direct connection to the Tonga plume depicted in dark colour at the same altitude across the equator.

No peak around this altitude was seen again before the measurement on October 5. Starting in October elevated aerosol was found around and below 20 km and below 25 km. In Fig. 17 we show the scattering ratios for four selected measurements from the period between October 2022 and February 2023. The relative importance varies with time, a minimum was found for the end of December and January. This (and the changing
505 tropopause) explains the strong variation of the integrated backscatter coefficients in Fig. 3.

On 19 October for the first time a particularly pronounced peak structure was retrieved (Fig. 17). This is confirmed by an OMPS aerosol curtain (Fig. 18). We prefer to display the extinction coefficients instead of the extinction ratio for more clearness. This reduces the sensitivity for the aerosol structures in the northern hemisphere. As in Fig. 16 the stratospheric aerosol maximizes in the tropics and the southern hemisphere, as one
510 would expect from the position of the Tonga archipelago. The x-shaped crosses at 25 km indicate a separate aerosol layer, slightly above the lidar peak.

Also during the following months the lidar aerosol maxima are located below the OMPS crosses. Around the latitude of UFS (47.5° N) no cross exists anyway, in agreement with lower structures in the UFS backscatter coefficients. Figure 19 shows the situation for 12 February 2023: The OMPS aerosol below 20 km had grown
515 considerably, which is confirmed by the pronounced peak for 12 February in Fig. 19. The corresponding OMPS extinction ratio (not shown) exceeds the colour scale in that image.

Motivated by the results of Vömel et al. (2022) we inspected the relative humidity (RH) distribution in the Munich radiosonde data. Normally, the RH values of the RS41 sonde launched by DWD decrease to 1 % within a few kilometres above the tropopause, 1 % mostly being the lowest value listed. Starting in October 2022 RH \geq
520 2 % became more and more frequent. By February 2023, the maximum RH ranged between 3 % and 5 %, 12 % on 13 February. The range of particularly elevated humidity was located clearly above the aerosol maximum.

The elevated RH values are strongly indicative of the Tonga plume. However, the RH maxima are located above the aerosol maxima. However, Khaykin et al. (2022b) demonstrated that the humidity layers may differ in altitude from layers with depolarizing particles.

525 Measurements with our Raman lidar (Klanner et al., 2021) in February 2023 indicate an increase of the water-vapour mixing ratio above 17 to 20 km, with an indication of further rise towards higher altitudes. However, the laser power was low which resulted in strongly enhanced uncertainty starting in this altitude range. and we prefer not to emphasize these findings.

530 The stratospheric aerosol quickly diminished in summer 2023. The upper boundary in October 2023 was roughly 26 km. This changed on 11 November, when we surprisingly observed some aerosol structure up to 34 km. The backscatter coefficients at the high altitudes were not strong which seems to exclude a fresh powerful eruption. Thus, we speculate on a return of the Hunga Tonga plume. Given the resubmission deadline we did not analyse this further.

4. Discussion and Conclusions

535 With the new lidar at UFS the long-term Garmisch-Partenkirchen stratospheric aerosol series has been continued since March 2016. The signal-to-noise ratio of the system has greatly improved allowing a better performance for 7.5-m vertical bins than previously with 75-m bins. The data evaluation, based on a Klett algorithm, now starts at $r = 45$ km ($h = 47.7$ km), but this could be extended even to larger distances. The limit is given by the NCEP pressure and temperature data used for the calibration of the aerosol backscatter coefficients that end
540 before 55 km a.s.l.

The integrated aerosol backscatter coefficients (Fig. 3) are dominated by the contributions from the first kilometres above the tropopause. Here, particles from moderate mid- and high-latitude volcanic eruptions, pyroCbs, desert dust (Trickl et al., 2013) and aircraft emissions cause a pronounced variability, sometimes featuring a spiky structure. These aerosols are removed at short to moderate time scales by stratosphere-to-
545 tropopause transport (e.g., tropopause folding, Fig. 6; Stohl et al., 2003) and dilution. Above 25 km the aerosol contributions in our data mostly disappear within less than 1.5 years. After the removal at low and high altitudes the maximum scattering ratio is typically observed around 20 km.

Vernier et al. (2013) concluded from satellite-based measurements that a calibration of an aerosol lidar with stratospheric capability must take place beyond 40 km. This is definitely true for tropical stations where the
550 aerosol is likely to extend to higher altitudes than in the mid-latitudes. Indeed, the Mauna Loa lidar observations quite often show aerosol at 37 to 38 km (John Barnes, personal communication, 2021). However, for our mid-latitude station we normally find upper boundaries of the aerosol between 25 and 30 km. In any case, given the performance of the new system, we are now prepared for periods with minor amounts of aerosol reaching to at least 35 km as found during a one-year period in recent years (see below).

555 The background phase 1999 to 2008 was rather special. The particularly low integrated backscatter coefficients during that period yielded integrated backscatter coefficients down to about 40 % of the 1979 average background (horizontal line in Fig. 3) that were never reached again later on. Most likely, the 1979 background did not represent a minimum during that period because of the tropical Fuego eruption in 1974. The very

560 remarkable aerosol depletion on some measurement days calls for more elaborate analysis of the reasons, such as troposphere-to-stratosphere transport (TST).

Indeed, TST was observed by us in a few cases in recent years and resulted in low aerosol up to a few kilometres above the tropopause (not presented here). For example, the occurrence of TST has been associated with upward transport in warm conveyor belts (WCBs; e.g., Stohl and Trickl, 1999; Trickl et al., 2003). Stohl (2001) and Madonna et al. (2014) estimated that overshoots of WCB air into the stratosphere can reach 10 % or more. In 565 addition, frequent vertical exchange between the troposphere and the stratosphere occurs along the subtropical jet stream (Sprenger et al., 2003; Trickl et al., 2011).

Aerosol sources were not completely absent during the low-background period, in particular strong eruptions in the tropics (Massie, 2016), but obviously did not significantly influence our observations. Most relevant for our station are mid-latitude eruptions to at least 10 km (Table 1 of Trickl et al., 2013). However, mid-latitude events 570 with layer tops of 12 km and more did not occur before 2006.

After the background phase there were two periods with clearly enhanced stratospheric loading, 2008 to 2012 and since 2017, which is the most spectacular phase since the Pinatubo eruption. In 2020 and early 2021 some aerosol extended to more than 35 km, tentatively ascribed to the tropical Ulawun eruption. This would be supported by Stenchikov et al. (2021) who report a maximum altitude of 35 km on the basis of model 575 calculations and SAGE data (cited by these authors as: Thomasson and Peter, 2006), after a rise from initial 17-26 km (Winker and Osborn, 1992; Guo et al., 2004).

It is interesting to compare this case with the more violent burst of Pinatubo. We, thus, inspected the evaluated profiles for 1991 to 1995 and mostly found rather sharp cut-offs near 30 km. Resolvable aerosol backscatter coefficients up to $2 \times 10^{-9} \text{ m}^{-1} \text{ sr}^{-1}$ (given the 75-m bin size chosen for the photon counter) rarely extend to more 580 than 32 km.

The absence of discernible aerosol contributions beyond 32 km during the Pinatubo period suggests to be careful in the 2020 case. One possible explanation could be a temporary offset of the NCEP data. However, it is difficult to assume such a bias for more than a year. Other sources, particularly the record-setting Australian fires are less realistic since they started in late December 2019 (Khaykin et al., 2020). This is too late to justify an impact on 585 our observations, at least in early 2020.

As an additional stratospheric contribution to the 2019 eruptions Ohneiser et al. (2021) report large Siberian fires in July and August 2019. They observed the plume in the polar vortex up to 18 km by lidar measurements onboard the research vessel Polarstern between October 2019 and May 2020. The origin of the particles in these fires was concluded by a high lidar ratio of 85 sr at 532 nm. Without the planned high-spectral-resolution 590 channel we could not fully answer the question on how much of the Siberian smoke passed over our station at just 45.455° N.

The observations of enhanced stratospheric aerosol in the Arctic could provide an answer to the question why the integrated backscatter coefficient decreased so slowly in 2020. Grooß and Müller (2021) report a particularly stable Arctic vortex and a pronounced ozone hole until early April 2020. This could have led to a retarded 595 outflow of aerosol-loaded air from the vortex. Indeed, the HYSPLIT trajectories for our two measurement days 7 April and 15 April show a transition from almost circular vortex to one with a more folded structure. The

tropopause was rather high in March and April which reduces the integrated backscatter coefficients, but Fig. 3 reveals an upward step.

600 Since 2017 a sudden increase of violent pyro-Cbs injecting smoke into the stratosphere has contributed to our observations. Indeed, Peterson et al. (2021) report an increasingly large stratospheric influence of pyroCbs. Khaykin et al. (2020) report on Australian fires up to 35 km. In our time series (Fig. 3) the first pronounced contribution of a pyroCb was the Québec fire in May and June 1991 (Fromm et al., 2010) just preceding the arrival of the Pinatubo plume and, therefore, initially not correctly identified (Carnuth et al., 2002). The recent rather sudden rise in strong loading of the stratosphere with particles from biomass burning up to even more than 605 20 km suggests further research. It is interesting to note in this context that the area burnt in the U.S. discussed by Trickl et al. (2013) has no longer increased since 2005.

During the period 2017 to present, discussed in this paper, there have been several opportunities to study the depletion of stratospheric aerosol. The depletion is mainly due to stratosphere-to-troposphere transport from the tropopause region, dilution (Fromm et al., 2008), advection of clean air masses (Vernier et al., 2011c; Khaykin et al., 2017) or sedimentation (Kremser et al., 2016). Unfortunately, the aerosol injections into the stratosphere were too frequent to allow us to observe a depletion down to the lowest values in the time series. As obvious from Fig. 3 the stratospheric aerosol loss in the case of mid-latitude eruption of Mt. St. Helens in 1980 occurred within a single year. Also after the first British Columbia pyro-Cb in 2017 the recovery of the stratosphere occurred within less than one year. The decay after the Raikoke eruption was much slower. It is reasonable to 610 assume that additional aerosol contributions reached the stratosphere during that period, such as the tropical Ulawun eruption. What we realized in 2021 and 2022 is that aerosol depletion took place first at high altitudes and then also just above the tropopause.

We are glad that more and more sources of stratospheric aerosol can be identified by following satellite measurement curtains or transport modelling or a combination of both. A special success was the identification 620 of the Tonga plume in our profiles. The tools meanwhile available on the internet, in particular transport models such as HYSPLIT or FLEXPART (<https://www.flexpart.eu/>), make possible an interpretation of the observations in much more detail than a few decades ago. Still, it is a challenge to follow plumes that have been in the stratosphere for more than the two weeks for which transport modelling in the free troposphere and stratosphere is applicable (e.g., Trickl et al., 2011; 2015) such as in the case of transport from the tropics to the mid-latitudes. 625 However, the growing information on strong aerosol sources allows one to determine the origin of pronounced features in the retrieved aerosol distributions.

5 Appendix

Rayleigh scattering

630 The calculation of the Rayleigh backscatter coefficients can be done with a relative uncertainty of about 0.5 % in the visible spectral range for a careful approach, if the atmospheric density is known with sufficient reliability. The details of Rayleigh scattering as applied in the IFU lidar algorithms are described in a review prepared in 2013 for the NDACC Lidar Working Group (“ISSI Team”, Leblanc et al. 2016a, b; meetings held at the Inter-

national Space Science institute, Bern, Switzerland) that is available in a revised version on the internet (Trickl, 2023). Because of the importance for the NDACC quality assurance we describe here a few important facts.

635 The total particle-free atmospheric scattering cross section is (in slight modification of Goody, 1964)

$$\sigma_R = \frac{24\pi^3}{\lambda^4 N^2} \frac{(n^2 - 1)^2}{(n^2 + 2)^2} F_K \quad (1)$$

with the refractive index n of air, the air density N and the King correction factor F_K . that implies the influence of Raman scattering. We traditionally (Kempfer et al., 1994) take the refractive index of air from a computer program reproducing the algorithm of Owens (1967) that provides the refractivity of air with an relative
640 uncertainty of about 10^{-8} , including CO_2 and humidity. The calculations of $n - 1$ are based on the Lorentz-Lorentz formalism, which, consequently, was adopted also in Eq. 1. This ensures that σ_R is constant as a function of the air density to within 7×10^{-7} .

Introducing the isotropic part α of the polarizability the leading term can also be written as (e.g., She, 2001)

$$\frac{8\pi}{3} \frac{\pi^2}{\lambda^4} \alpha^2 = \frac{24\pi^3}{\lambda^4 N^2} \frac{(n^2 - 1)^2}{(n^2 + 2)^2}, \quad (2)$$

645 neglecting wavelength differences.

Bates (1984) lists $F_K - 1$ for wavelengths from 200 nm to 1000 nm with an estimated relative uncertainty of 1 % (about 0.5 % visible spectral region). A least-squares fit to the $F_K - 1$ of these values using the expression

$$F_K - 1 = \sum_{i=0}^2 p_i \lambda^{-2i}, \quad (3)$$

λ in nm, yields the fit parameters (in brackets: relative standard uncertainties):

650 $p_0 = 4.69541179 \times 10^{-2}$ (3.49×10^{-3}), $p_1 = 3.25031532 \times 10^{+2}$ (1.06×10^{-1}), $p_2 = 3.86228507 \times 10^{+7}$ (3.63×10^{-2}).

The $F_K - 1$ data are approximated by Eq. 1 mostly within clearly less than 1 % between 200 nm and 1000 nm, respectively, implying a negligible relative deviation for F_K . The 532.24-nm backward differential cross section without Raman contribution is $5.86612 \times 10^{-32} \text{ m}^{-2}$, the King factor $F_K = 1.048583$.

In the backward direction the correction factor is

655 $F_K(\pi) = 1 + 0.7(F_K - 1)$ (4)

The factor 0.7 differs from the value 1.0 used in many lidar applications. In the classical theory for polarized scattered radiation and unpolarized detection the differential backscatter cross section for the Q branch component of the central (Cabannes) line is

$$\frac{d\sigma_Q}{d\Omega}(\pi) = 0.25 \frac{\pi^2}{\lambda^4} \alpha^2 [0.7(F_K - 1)] = 0.25 \frac{\pi^2}{\lambda^4} \alpha^2 \left[\frac{7}{45} \frac{\gamma^2}{\alpha^2} \right], \quad (5)$$

660 γ being the anisotropic part of the polarizability. For the quantum solution just a small correction is needed for the first factor: For example, for $T = 280 \text{ K}$ we derive 0.25545 (nitrogen) and 0.26015 (oxygen), the sum over all

three rotational branches being 1.0000 (Trickl, 2023). The sum of S and O branch relative line strengths is just slightly below 0.75.

665 The influence of the interference filter in the far-field channel was estimated by calculating the nitrogen Raman spectrum from spectroscopic data (Placzek and Teller, 1933; Herzberg, 1950; Trickl et al., 1993; 1995). A relative contribution of the S and O branches of just 3 % of the full sum of about 0.75 of the relative O- and S-branch line strengths was determined for the 0.5-nm width of the spectral filter in the far-field channel of the receiver. This fraction is taken for the data evaluation in the filtered channel, but the influence in the retrieval is small in comparison with the overall uncertainty.

670 *Uncertainties*

Although uncertainties of the backscatter coefficients have been determined in the past (Jäger, 2005) it is important to give, for the first time, a few more details, from the current point of view. The highest contribution to the uncertainty budget is caused by the calibration of the Klett retrieval. The sensitivity of the backscatter coefficients to the far-field calibration of is extreme because of the mostly very small values of the Rayleigh
675 backscatter coefficients above the aerosol layer and the noise of the backscatter signal. Any deviation from the best Rayleigh fit is interpreted as aerosol. In the range of zero aerosol backscatter coefficients typically down to 30 km the result must be perfectly centred in the noise (Fig. 1) in order to avoid a bias at altitudes below 30 km that can readily reach 10 % and more otherwise.

The uncertainty of the air density is rather low. During the period under consideration the RS92 and RS41
680 radiosondes from Vaisala have been used by the German Weather Service (DWD). Steinbrecht et al. (2008) carefully examined the RS80 and RS92 sondes in twin flights. The RS92 sonde turned out to be more accurate and we assume a similar performance for RS41. The relative uncertainties of RS92 for temperature and altitude are clearly below 1 % and, thus, do not contribute significantly to that of the air density. The pressure uncertainty matters most at low pressures. Between 100 and 3 mbar it is specified as 0.3 mbar which means a relative
685 uncertainty of 3 % for the air density at the beginning of the calibration range of the lidar.

However, Rayleigh backscatter profiles calculated from the corresponding midnight sonde and the noon NCEP data have perfectly matched the photon-counting backscatter profiles for all low-noise measurements. The photon-counting channel is virtually free of any artefact. The high reliability could be further hardened by the one-hour temperature measurements even exceeding the range of the NCEP data (Klanner et al., 2021). Up to 53
690 km a.s.l., where the NCEP data ended in that case, the agreement with the lidar-based temperature was within 2 (≤ 35 km) to 4 K (53 km). In the case discussed the temperature deviation was caused by a positive altitude offset of the NCEP data growing from 0 to 2 km between 40 and 53 km. More recent measurements demonstrated similar to better agreement. Therefore, the relative uncertainty of the NCEP data is of the order of 1 % and less.

695 Another source of uncertainty is the variability of stratospheric ozone. The maximum monthly mean ozone density in the MOHp analysis is located at 22 km, where we also see largest influence in the retrievals shown in Fig. 2. The monthly standard deviations evaluated for the MOHp ozone-sonde data range between 4.2 % (October) and 8.6 % (February). This yields a contribution much smaller than the overall uncertainty of the lidar retrieval.

700 The influence of the lidar ratio on the result of a stratospheric retrieval is small and, as mentioned, is based on values close to the recommended ones. However, there is a strong difference in the case of the extreme biomass-burning case on 25 August 2017. For this day we used a lidar ratio of 70 sr^{-1} in the thin layer (Sect. 3.2) as determined by Ansmann et al. (2018). The backscatter coefficients below the plume decreased by about 20 % and then matched those above the layer.

705 For the integrated aerosol backscatter coefficients the chosen position of the tropopause is crucial because the highest contributions occur in the tropopause region. Mostly, the Munich tropopause looks very reasonable. However, as pointed out above, refinement is sometimes necessary. Without additional aerosol features at higher altitudes the highest values of the backscatter coefficients are found in the tropopause region. Thus, the choice of the tropopause is made with care (Sect. 2.2), based on the observations. The uncertainty of the integrated
710 backscatter coefficients due to that of the tropopause normally does not exceed 10 %.

Cirrus clouds no longer influence the far-field signal with the 7400 PMT. In the past, signal induced nonlinearities were observed in the stratosphere if the EMI PMTs were overloaded even by big cirrus spikes in the tropopause region. Multiple scattering effects must be taken into consideration (Reichardt and Reichardt, 2006). They, indeed, exist in the case of thick cirrus clouds in the 313-nm channel of our ozone DIAL, but could
715 not be verified in the green channel of the system described here except for a few extreme cases.

Leblanc et al. (2016b) derived a very complex approach to the determination of uncertainties. We strongly reduce the complexity by parametrizing the uncertainty u as

$$u = \sqrt{u_0^2 + \left(u_1 \frac{r^2}{r_{ref}^2}\right)^2 + (u_2 S(r))^2}$$

The three coefficients u_0 , u_1 and u_2 are adjusted by sensitivity analyses, separately for all three data channels taken (see Fig. 1 and the related explanations in Sect. 2.2).
720

We rather conservatively assume a minimum relative uncertainty of 15 % of the aerosol backscatter coefficient (u_2) until more experience is available. This approach chosen has entered the uncertainties archived in the NDACC data base for the measurements since 2012.

6 Data availability

725 The 532-nm backscatter coefficients retrieved from the lidar measurements have been archived in the NDACC data base (actual web address: <https://www-air.larc.nasa.gov/missions/ndacc/data.html#>). Until January 2016, the station name is “Garmisch”, afterwards “Zugspitze”. The data are also available under https://doi.org/10.60897/garmisch_v01_lidar and https://doi.org/10.60897/zugspitze_v01_lidar, respectively.

The backscatter coefficients from 2000 until January 2016 are also stored in the EARLINET data base
730 (<https://data.earlinet.org/earlinet/login.zul;jsessionid=E798A6771CDCF8034934538F567C8E25>).

7 Author statement

735 TT evaluated the data. He interpreted the observations and wrote the paper, assisted by HF, MF and HJ. HV carried out the lidar measurements since 2016. HJ provided the information on the Pinatubo period. HV and MP built and optimized the new lidar at UFS, including the remote system control. WS contributed the climatological ozone profiles from Hohenpeißenberg sonde and lidar vertical soundings.

8 Competing interests

740 The authors declare that they have no conflict of interest.

Acknowledgements

The authors thank Hans Peter Schmid for his support to continue the measurements. They acknowledge the appreciation of this effort by their NDACC and EARLINET colleagues. It is important to mention the contributions of Walther Carnuth († May 2021), Helmuth Giehl and Stefan Biggel in different stages of the measurements. The technical improvements would not have been possible without the contributions of Werner Funk, Bernd Mielke, Heinz Josef Romanski and Bernhard Stein. Ludwig Ries made available the UFS ozone data. This work has contributed to NDACC and EARLINET, the latter now being a part of the European research infrastructure ACTRIS.#Ann Mari Fjæraa and the ESA (European Space Agency) Atmospheric Validation Data Centre made available access to the DOIs.

745

750 The publication of this article has been supported by the Helmholtz Association within its open-access initiative.

References

- Ancellet, G., Pelon, J., Totems, J., Chazette, P., Bazureau, A., Sicard, M., Di Iorio, T., Dulac, F., and Mallet, M.: Long-range transport and mixing of aerosol sources during the 2013 North American biomass burning episode: analysis of multiple lidar observations in the western Mediterranean basin, *Atmos. Chem. Phys.*, 16, 4725–4742, www.atmos-chem-phys.net/16/4725/2016/ doi:10.5194/acp-16-4725-2016, 2016.
- Ansmann, A., Mattis, I., Wandinger, U., Wagner, F., Reichardt, J., and Deshler, T.: Evolution of the Pinatubo Aerosol: Raman Lidar Observations of Particle Optical Depth, Effective Radius, Mass, and Surface Area over Central Europe at 53.48° N, *J. Atmos. Sci.*, 54, 2630–2641, [https://doi.org/10.1175/1520-0469\(1997\)054<2630:EOTPAR>2.0.CO;2](https://doi.org/10.1175/1520-0469(1997)054<2630:EOTPAR>2.0.CO;2), 1997.
- Ansmann, A., Baars, H., Chudnovsky, A., Mattis, I., Veselovskii, I., Haarig, M., Seifert, P., Engelmann, R., and Wandinger, U.: Extreme levels of Canadian wildfire smoke in the stratosphere over central Europe on 21–22 August 2017, *Atmos. Chem. Phys.*, 18, 11831–11845, <https://doi.org/10.5194/acp-18-11831-2018>, 2018
- Ansmann, A., Ohneiser, K., Chudnovsky, A., Baars, H., and Engelmann, R.: CALIPSO Aerosol-Typing Scheme Misclassified Stratospheric Fire Smoke: Case Study From the 2019 Siberian Wildfire Season, *Front. Environ. Sci.*, 9:769852, 13 pp., 2021, doi: 10.3389/fenvs.2021.769852.
- Bates, D. R.: Rayleigh Scattering by Air, *Planet. Space Sci.*, 32, 785–790, 1984.
- Baars, H., Ansmann, A., Ohneiser, K., Haarig, M., Engelmann, R., Althausen, D., Hanssen, I., Gausa, M., Pietruczuk, A., Szkop, A., Stachlewska, I., Wang, D., Reichardt, J., Skupin, A., Mattis, I., Trickl, T., Vogelmann, H., Navas-Guzmán, F., Haeffele, S., Acheson, K., Ruth, A. A., Tatarov, B., Müller, D., Hu, Q., Podvin, T., Goloub, P., Vesselovski, I., Pietras, C., Haeffelin, M., Fréville, P., Sicard, M., Comerón, A., Fernández García, A. J., Molero Menéndez, F., Córdoba-Jabonero, C., Guerrero-Rascado, J. L., Alados-Arboledas, L., Bortoli, D., Costa, M. J., Dionisi, D., Liberti, G., Wang, X., Sannino, A., Papagiannopoulos, N., Boselli, A., Mona, L., D'Amico, G., Romano, S., Perrone, M. R., Belegante, L., Nicolae, D., Grigorov, I., Gialitaki, A., Amiridis, V., Soupiona, O., Papayannis, A., Mamouri, R.-E., Nisantzi, A., Heese, B., Hofer, J., Schechner, Y. Y., Wandinger, U., and Pappalardo, G.: The unprecedented 2017–2018 stratospheric smoke event: Decay phase and aerosol properties observed with the EARLINET, *Atmos. Chem. Phys.*, 19, 15183–15198, 2019.
- Bingen, C., Robert, C. E., Stebel, K., Brühl, C., Schallock, J., Vanhellefont, F., Mateshvili, N., Höpfner, M., Trickl, T., Barnes, J. E., Jumelet, J., Vernier, J.-P., Popp, J., de Leeuw, G., and Pinnock, S.: Stratospheric aerosol data records for the climate change initiative: Development, validation and application to chemistry-climate modelling, *Remote Sensing of Environment*, 203, 296–321, 2017.
- Bösenberg, J., Matthias, V., Amodeo, A., Amiridis, V., Ansmann, A., Baldasano, J. M., Balin, I., Balis, D., Böckmann, C., Boselli, A., Carlsson, G., Chaikovski, A., Chourdakis, G., Comerón, A., De Tomasi, F., Eixmann, R., Freudenthaler, V., Giehl, H., Grigorov, I., Hågård, A., Iarlore, M., Kirsche, A., Kolarov, G., Komguem, L., Kreipl, S., Kumpf, W., Larchevêque, G., Linné, H., Matthey, R., Mattis, I., Mekler, A., Mironova, I., Mitev, V., Mona, L., Müller, D., Music, S., Nickovic, S., Pandolfi, M., Papayannis, A., Pappalardo, G., Pelon, J., Pérez, C., Perrone, R. M., Persson, R., Resendes, D. P., Rizi, V., Rocadenbosch, F.,

- Rodrigues, J. A., Sauvage, L., Schneidenbach, L., Schumacher, R., Sherbakov, V., Simeonov, V., Sobolewski, P., Spinelli, N., Stachlewska, I., Stoyanov, D., Trickl, T., Tsaknakis, G., Vaughan, G., Wandinger, U., Wang, X., Wiegner, M., Zavrtnik, M., and Zerefos, C.: EARLINET: A European Aerosol Research Lidar Network to Establish an Aerosol Climatology, J. Bösenberg, Co-ordinator, Max-Planck-Institut für Meteorologie (Hamburg, Germany), Report Nr. 348, ISSN 0937 1060, 155 pp., 2003.
- Boone, C. D., Bernath, P. F., Labelle, K., and Crouse, J.: Stratospheric Aerosol Composition Observed by the Atmospheric Chemistry Experiment Following the 2019, Raikoke Eruption, *J. Geophys. Res.*, 127, e2022JD036600. <https://doi.org/10.1029/2022JD036600>, 16 pp., 2022.
- Brion, J., Chakir, A., Charbonnier, J., Daumont, D., Parisse, C., and Malicet, J.: Absorption Spectra Measurements for the Ozone Molecule in the 350-830 nm Region, *J. Atmos. Chem.*, 30, 291-299, 1998.
- Browell, E. V., Danielsen, E. F., Ismail, S., Gregory, G. L., and Beck, S. M.: Tropopause Fold Structure Determined from Airborne Lidar and in Situ Measurements, *J. Geophys. Res.* 92, 2112-2120, 1987.
- Butchart, N.: The Brewer-Dobson circulation, *Rev. Geophys.*, 157–184, doi:10.1007/s00382-006-0162-4, 2014.
- Butchart, N., Scaife, A. A., Bourqui, M., de Grandpré, J., Hare, S. H. E., Kettleborough, J., Langematz, U., Manzini, E., Sassi, F., Shibata, K., Shindell, D., and Sigmond, M.: Simulations of anthropogenic change in the strength of the Brewer–Dobson circulation, *Clim. Dyn.*, 27, 727–741, 2006.
- Cameron, W. D., Bernath, P., and Boone, C.: Sulfur dioxide from the atmospheric chemistry experiment (ACE) satellite, *J. Quant. Spectrosc. Radiat. Transf.*, 258, 107341, 11 pp., 2021.
- Carnuth, W. and Trickl, T.: Transport studies with the IFU three-wavelength aerosol lidar during the VOTALP Mesolcina experiment, *Atmos. Environ.*, 34, 1425-1434, 2000.
- Carnuth, W., Kempfer, U., and Trickl, T.: Highlights of the Tropospheric Lidar Studies at IFU within the TOR Project, *Tellus B*, 54, 163-185, 2002.
- Chouza, F., Leblanc, T., Barnes, J., Brewer, M., Wang, P., and Koon, D.: Long-term (1999–2019) variability of stratospheric aerosol over Mauna Loa, Hawaii, as seen by two co-located lidars and satellite measurements, *Atmos. Chem. Phys.*, 20, 6821–6839, <https://doi.org/10.5194/acp-20-6821-2020>, 2020.
- de Laat, A. T. J., Stein Zweers, D. C., Boers, R., and Tuinder, O. N. E.: A solar escalator: Observational evidence of the self-lifting of smoke and aerosols by absorption of solar radiation in the February 2009 Australian Black Saturday plume, *J. Geophys. Res.*, 117, D04204, <https://doi.org/10.1029/2011JD017016>, 2012.
- Deshler, T., Anderson-Sprecher, R., Jäger, H., Barnes, J., Hofmann, D. J., Clemesha, B., Simonich, D., Osborn, M., Grainger, R. G., and Godin-Beekmann, S.: Trends in the nonvolcanic component of stratospheric aerosol over the period 1971–2004, *J. Geophys. Res.*, 111, D01201, doi:10.1029/2005JD006089, 21 pp., 2006.
- Deshler, T.: A review of global stratospheric aerosol: Measurements, importance, life cycle, and stratospheric aerosol, *Atmos. Res.*, 90, 223-232, 2008.
- Draxler, R., and Hess, G.: An overview of the HYSPLIT_4 modelling system for trajectories, dispersion, and deposition, *Aust. Meteorol. Mag.*, 47, pp. 295-308, 1998.
- Eisele, H., and Trickl, T.: Improvements of the aerosol algorithm in ozone-lidar data processing by use of evolutionary strategies, *Appl. Opt.*, 44, 2638-2651, 2005.

- Forster, C., Wandinger, U., Wotawa, G., James, P., Mattis, I., Althausen, D., Simmonds, P., O'Doherty, S., Jennings, S. G., Kleefeld, C., Schneider, J., Trickl, T., Kreipl, S., Jäger, H., and Stohl, A.: Transport of boreal forest fire emissions from Canada to Europe, *J. Geophys. Res.*, 106, 22887-22906, 2001.
- Freudenthaler V.: Lidarmessungen der räumlichen Ausbreitung sowie mikrophysikalischer und optischer Parameter von Flugzeugkondensstreifen, Dissertation, Universität Hohenheim, Germany (1999) und Schriftenreihe des Fraunhofer-Instituts für Atmosphärische Umweltforschung, Vol. 63, 134 pp., Shaker Verlag GmbH (Aachen, 2000), ISBN 3-8265-6973-3, ISSN 1436-1094; in German.
- Freudenthaler V., Homburg, F., and Jäger, H.: Ground-based mobile scanning LIDAR for remote sensing of contrails, *Ann. Geophysicae*, 12, 956-961, 1994.
- 835 Freudenthaler, V., Homburg, F., and Jäger, H.: Contrail observations by ground-based mobile scanning lidar: cross-sectional growth, *Geophys. Res. Lett.*, 22, 3501-3504, 1995
- Fromm, M., and Servranckx, R.: Transport of forest fire smoke, above the tropopause, supercell convection, *Geophys. Res. Lett.*, 30, 1542, doi: 10.1029/2002GL016820, 4 pp., 2003.
- Fromm, M., Alfred, J., Hoppel, K., Hornstein, J., Bevilacqua, R., Shettle, E., Servranckx, R., Li, Z., and Stocks, B.: Observations of boreal forest fire smoke in the stratosphere by POAM III, SAGE II, and lidar in 1998, *Geophys. Res. Lett.*, 27, pp. 1407– 1410, 2000.
- 840 Fromm, M., Torres, O., Diner, D., Lindsey, D., Vant Hull, B., Servranckx, R., Shettle, E. P., and Li, Z.: Stratospheric impact of the Chisholm pyrocumulonimbus eruption: 1. Earth-viewing satellite perspective, *J. Geophys. Res.*, 113, D08202, doi:10.1029/2007JD009153, 16 pp., 2008a.
- 845 Fromm, M., Shettle, E. P., Fricke, K. H., Ritter, C., Trickl, T., Giehl, H., Gerding, M., Barnes, J., O'Neill, M., Massie, S. T., Blum, U., McDermid, I. S., Leblanc, T., and Deshler, T.: The stratospheric impact of the Chisholm PyroCumulonimbus eruption: 2. Vertical profile perspective, *J. Geophys. Res.*, 113, D08203, doi: 10.1029/2007JD009147, 19 pp., 2008b.
- Fromm, M., Lindsey, D. T., Servranckx, R., Yue, G., Trickl, T., Sica, R., Doucet, P., and Godin-Beekmann, S.: 850 The Untold Story of Pyrocumulonimbus, *Bull. Am. Meteorol. Soc.*, 91, 1193-1209, 2010.
- Fromm, M., Peterson, D., and Di Girolamo, L.: The Primary Convective Pathway for Observed Wildfire Emissions in the Upper Troposphere and Lower Stratosphere: A Targeted Reinterpretation, *J. Geophys. Res.*, 124, 1-9, <https://doi.org/10.1029/2019JD031006>, 2019.
- Fromm, M. D., Kablick, G. P., Peterson, D. A., Kahn, R. A., Flower, V. J. B., and Seftor, C. J.: Quantifying the 855 Source Term and Uniqueness of the August 12, 2017 Pacific Northwest PyroCb Event, *J. Geophys. Res.*, 126, e2021JD034928. <https://doi.org/10.1029/2021JD034928>, 25 pp., 2021.
- Fromm, M., Servranckx, R., Stocks, B. J., and Peterson, D. A.: Understanding the critical elements of the pyrocumulonimbus storm sparked by high-intensity wildland fire, *Comm. Earth and Environ.*, 3:243, <https://doi.org/10.1038/s43247-022-00566-8>, 7 pp., 2022.
- 860 Goody, R. M.: Extinction by Molecules and Droplets, Sec. 7 in: *Atmospheric Radiation*, Vol. 1, Theoretical Basis, Oxford at the Clarendon Press (Oxford, U.K.), pp. 286-318, 1964.

- Groß, J.-U., and Müller, R.: Simulation of Record Arctic Stratospheric Ozone Depletion in 2020, *J. Geophys. Res.*, 126, e2020JD033339. <https://doi.org/10.1029/2020JD033339>, 17 pp., 2021.
- Guo, S., Bluth, G. J. S., Rose, W. I., Watson, I. M., and Prata, A. J.: Re-evaluation of SO₂ release of the 15 June 1991 Pinatubo eruption using ultraviolet and infrared satellite sensors. *Geochem., Geophys., Geosyst.*, 5. <https://doi.org/10.1029/2003gc000654>, 2004.
- Herzberg, H.: *Molecular Spectra and Molecular Structure, I. Spectra of Diatomic Molecules*, van Nostrand Reinhold (New York, 1950)
- Hofmann, D., Barnes, J., O'Neill, M., Trudeau, M., and Neely, R.: Increase in background stratospheric aerosol observed with lidar at Mauna Loa Observatory and Boulder, Colorado, *Geophys. Res. Lett.*, 36, L15808, doi: 10.1029/2009GL039008, 5 pp., 2009.
- Holton, J. R., Haynes, P. H., McIntyre, M. E., Douglass, A. R., Rood, R. B., and Pfister, L.: Stratosphere-troposphere exchange, *Rev. Geophys.*, 33, 403–439, 1995.
- Hoyle, C. R., Engel, I., Luo, B. P., Pitts, M. C., Poole, L. R., Groß, J.-U., and Peter, T.: Heterogeneous formation of polar stratospheric clouds – Part 1: Nucleation of nitric acid trihydrate (NAT), *Atmospheric Chemistry and Physics*, 13, 9577–9595, <https://doi.org/10.5194/acp-13-9577-2013>, 2013.
- Hu, Q., Goloub, P., Veselovskii, I., and Podvin, T.: The characterization of long-range transported North American biomass burning plumes: what can a multi-wavelength Mie–Raman-polarization-fluorescence lidar provide? *Atmos. Chem. Phys.*, 22, 5399–5414, 2022.
- Jäger, H.: Long-term record of lidar observations of the stratospheric aerosol layer at Garmisch-Partenkirchen, *J. Geophys. Res.*, 110, D08106, doi: 10.1029/2004JD005506, 9 pp., 2005.
- Jäger, H., Carnuth, W., and Georgi, B.: Observations of Saharan Dust at a North Alpine Station, *J. Aerosol Sci.*, 19, 1235-1238, 1988
- Jäger, H., James, P., Stohl, A., and Trickl, T.: Long-Range Transport of Free-Tropospheric Aerosol: A Nine-year Climatology, pp. 795 to 796 in: *Reviewed and Revised Papers Presented at the 23rd International Laser Radar Conference, Nara (Japan), July 24 to 28, 2006*, C. Nagasawa, N. Sugimoto, Eds., Tokyo Metropolitan University (Tokyo, Japan, 2006), ISBN 4-9902916-0-3
- Jäger, H., and Deshler, T.: Lidar backscatter to extinction, mass and area conversions for stratospheric aerosols based on midlatitude balloonborne size distribution measurements, *Geophys. Res. Lett.*, 29, 1929, doi: 10.1029/2002GL015609, 4 pp., 2002.
- Jäger, H., and Deshler, T.: Correction to "Lidar backscatter to extinction, mass and area conversions for stratospheric aerosols based on midlatitude balloonborne size distribution measurements", *Geophys. Res. Lett.*, 30, 1382, doi: 10.1029/2003GL017189, 1 p., 2003.
- Johnson, M. S., Strawbridge, K., Knowland, K. E., Keller, C., and Travis, M.: Long-range transport of Siberian biomass burning emissions to North America during FIREX-AQ, *Atmos. Environ.*, 252, 118241, <https://doi.org/10.1016/j.atmosenv.2021.118241>, 2021.
- Kempfer, U., Carnuth, W., Lotz, R., and Trickl, T.: A wide range ultraviolet lidar system for tropospheric ozone measurements: development and application, *Rev. Sci. Instrum.*, 65, 3145-3164, 1994.

- 900 Khaykin, S. M., Godin-Beekmann, S., Keckhut, P., Hauchecorne, A., Jumelet, J., Vernier, J.-P., Bourassa, A., Degenstein, D. A., Rieger, L. A., Bingen, C., Vanhellefont, F., Robert, C., DeLand, M., and Bhartia, P. K.: Variability and evolution of the midlatitude stratospheric aerosol budget from 22 years of ground-based lidar and satellite observations, *Atmos. Chem. Phys.*, 17, 1829–1845, <https://doi.org/10.5194/acp-17-1829-2017>, 2017.
- Khaykin, S. M., Godin-Beekmann, S., Hauchecorne, A., Pelon, J., Ravetta, F., and Keckhut, P.: Stratospheric Smoke With Unprecedentedly High Backscatter Observed by Lidars Above Southern France, *Geophys. Res. Lett.*, 45, 1639–1646. <https://doi.org/10.1002/2017GL076763>, 2018.
- 905 Khaykin, S., Legras, B., Bucci, S., Sellitto, P., Isaksen, L., Tence, F., Bekki, S., Bourassa, A., Rieger, L., Zawada, D., Jumelet, J., and Godin-Beekmann, S.: The 2019–2020 Australian wildfires generated a persistent smoke-charged vortex rising up to 35 km altitude, *Comm. Earth Environ.*, 1, 22, <https://doi.org/10.1038/s43247-020-00022-5>, 12 pp., 2020.
- 910 Khaykin, S. M., de Laat, A. T. J., Godin-Beekmann, S., Hauchecorne, A., and Ratynski, M.: Unexpected self-lofting and dynamical confinement of volcanic plumes: the Raikoke 2019 case, *Scientific Reports*, 22, 22409, <https://doi.org/10.1038/s41598-022-27021-0>, 12 pp., 2022a.
- Khaykin, S., Podglajen, A., Ploeger, F., Groß, J.-U., Tence, F., Bekki, S., Khlopenkov, K., Bedka, K., Rieger, L., Baron, A., Godin-Beekmann, S., Legras, B., Sellitto, P., Sakai, T., Barnes, J., Uchino, O., Morino, I., Nagai, T., Wing, R., Baumgarten, G., Gerding, M., Duflot, V., Payen, G., Jumelet, J., Querel, R., Liley, B., Bourassa, A., Clouser, B., Feofilov, A., Hauchecorne, A., and Ravetta, F.: Global perturbation of stratospheric water and aerosol burden by Hunga eruption, *Comm. Earth Environ.*, 3:316, 15 pp., <https://doi.org/10.1038/s43247-022-00652-x>, 2022b.
- 915 Klanner, L. Höveler, K., Khordakova, D., Perfahl, M., Rolf, C., Trickl, T., and Vogelmann, H.: A powerful lidar system capable of one-hour measurements of water vapour in the troposphere and the lower stratosphere as well as the temperature in the upper stratosphere and mesosphere, *Atmos. Meas. Tech.*, 14, 531–555, 2021.
- 920 Klett, J. D.: Lidar inversion with variable backscatter/extinction ratios, *Appl. Opt.*, 24, 1638–1643, 1985.
- Kloss, C., Berthet, G., Sellitto, P., Ploeger, F., Taha, G., Tidiga, M., Eremenko, M., Bossolasco, A., Jégou, F., Renard, J.-B., and Legras, B.: Stratospheric aerosol layer perturbation caused by the 2019 Raikoke and Ulawun eruptions and their radiative forcing, *Atmos. Chem. Phys.*, 21, 535–560, 2021.
- 925 Knepp, T. N., Thomason, L., Kovilakam, M., Tackett, J., Kar, J., Damadeo, R., and Flittner, D.: Identification of smoke and sulfuric acid aerosol in SAGE III/ISS extinction spectra, *Atmos. Meas. Tech.*, 15, 5235–5260, 2022.
- Kremser, S., Thomason, L. W., von Hobe, M., Hermann, M., Deshler, T., Timmreck, C., Toohey, M., Stenke, A., Schwarz, J. P., Weigel, R., Fueglistaler, S., Prata, F. J., Vernier, J.-P., Schlager, H., Barnes, J. E., Antuña-Marrero, J.-C., Fairlie, D., Palm, M., Mahieu, E., Notholt, J., Rex, M., Bingen, C., Vanhellefont, F., Bourassa, A., Plane, J. M. C., Klocke, D., Carn, S. A., Clarisse, L., Trickl, T., Neely, R., James, A. D., Rieger, L., Wilson, J. C., and Meland, B.: Stratospheric aerosol - Observations, processes, and impact on climate, *Rev. Geophys.*, 54, 278–335, doi: 10.1002/2015RG000511, 2016.
- 930 Lareau, N. P., Nauslar, N. J., Bentley, E., Roberts, M., Emmerson, S., Brong, B., Mehle, M., and Wallman, M.: Fire-Generated Tornadoic Vortices, *Bull. Am. Meteorol. Soc.*, 103, E1296–E1320, 2022.

- Leblanc, T., Sica, R. J., van Gijsel, J. A. E., Godin-Beekmann, S., Haeefe, A., Trickl, T., Payen, G., and Gabarrot, F.: Proposed standardized definitions for vertical resolution and uncertainty in the NDACC lidar ozone and temperature algorithms. Part 1: Vertical resolution, *Atmos. Meas. Tech.*, 9, 4029-4049; 18-pp. supplement, 2016a.
- 940 Leblanc, T., Sica, R. J., van Gijsel, J. A. E., Godin-Beekmann, S., Haeefe, A., Trickl, T., Payen, G., and Liberti, G.: Proposed standardized definitions for vertical resolution and uncertainty in the NDACC lidar ozone and temperature algorithms. Part 2: Ozone DIAL uncertainty budget, *Atmos. Meas. Tech.*, 9, 4051-4078, 2016b.
- Lestrelin, H., Legras, B., Podglajen, A., and Salihoglu, M.: Smoke-charged vortices in the stratosphere generated by wildfires and their behaviour in both hemispheres: comparing Australia 2020 to Canada 2017, *Atmos. Chem. Phys.*, 21, 7113–7134, <https://doi.org/10.5194/acp-21-7113-2021>, 2021.
- 945 Markowicz, K. M., Chilinski, M. T., Lisok, J., Zawadzka, O., Stachlewska, I. S., Janicka, L., Rozwadowska, A., Makuch, P., Pakszys, P., Zielinski, T., Petelski, T., Posyniak, M., Pietruczuk, A., Szkop, A., and Westphal, D. L.: Study of aerosol optical properties during long-range transport of biomass burning from Canada to Central Europe in July 2013, *J. Aerosol Sci.* 101, 156–173, 2016.
- 950 Rodanthi-Elisavet Mamouri, R.-E., Ansmann, A., Ohneiser, K., Knopf, D., Nisantzi, A., Buhl, J., Engelmann, R., Skupin, A., Seifert, P., Baars, H., Ene, D., Wandinger, U., and Hadjimitsis, D.: Wildfire smoke triggers cirrus formation: Lidar observations over the Eastern Mediterranean (Cyprus), <https://doi.org/10.5194/egusphere-2023-988>
- Massie, S. T.: "Summary of volcanic activity", AURA Cloud/Aerosol/SO₂ Working Group, release February 955 2016, received from the author.
- McCormick, M. P., Swisler, T. J., Chu, W. P., and Fuller, W. H.: Post-Volcanic Stratospheric Aerosol Decay as Measured by Lidar, *J. Atmos. Sci.*, 35, 1296-1303, 1978.
- Michailidis, K., Koukouli, M.-E., Balis, D., Veefkind, J. P., de Graaf, M., Mona, L., Papagianopoulos, N., Pappalardo, G., Tsikoudi, I., Amiridis, V., Marinou, E., Gialitaki, A., Mamouri, R.-E., Nisantzi, A., Bortoli, D., 960 Costa, M. J., Salgueiro, V., Papayannis, A., Mylonaki, M., Alados-Arboledas, L., Romano, S., Perrone, M. R., and Baars, H.: Validation of the TROPOMI/S5P aerosol layer height using EARLINET lidars, *Atmos. Chem. Phys.*, 23, 1919–1940, 2023, <https://doi.org/10.5194/acp-23-1919-2023>
- Mishra, M. K., Hoffmann, L., and Thapliyal, P. K.: Investigations on the Global Spread of the Hunga Tonga-Hunga Ha'apai Volcanic Eruption Using Space-Based Observations and Lagrangian Transport Simulations, 965 *Atmosphere*, 13, 2055, 23 pp., 2022.
- Müller, D., Mattis, I., Wandinger, U., Ansmann, A., Althausen, D., and Stohl, A.: Raman lidar observations of aged Siberian and Canadian forest fire smoke in the free troposphere over Germany in 2003: Microphysical particle characterization, *J. Geophys. Res.*, 110, D17201, doi:10.1029/2004JD005756, 16 pp., 2005
- Murphy, D.M., Froyd, K., D., Bourgeois, I., Brock, C. A., Kupc, A., Peischl, J., Schill, G. P., Thompson, C. R., 970 Williamson, C. J., and Yu, P.: Radiative and chemical implications of the size and composition of aerosol particles in the existing or modified global stratosphere, *Atmos. Chem. Phys.*, 21, 8915–8932, 2021.
- Newhall, C. G., and Self, S.: The volcanic explosivity index (VEI): an estimate of explosive magnitude for historical volcanism, *J. Geophys. Res.*, 87, 1231-38, 1982.

- Ohneiser, K., Ansmann, A., Chudnovsky, A., Engelmann, R., Ritter, C., Veselovskii, I., Baars, H., Gebauer, H.,
975 Griesche, H., Radenz, M., Hofer, J., Althausen, D., Dahlke, S., and Maturilli, M.: Siberian fire smoke in the
High Arctic winter stratosphere during MOSAiC 2019–2020, *Atmos. Chem. Phys.*, 21, 15783–15808,
<https://doi.org/10.5194/acp-21-15783-2021>, 2021.
- Ohneiser, K., Ansmann, A., Kaifler, B., Chudnovsky, A., Barja, B., Knopf, D. A., Kaifler, N., Baars, H., Seifert,
P., Villanueva, D., Jimenez, C., Radenz, M., Engelmann, R., Veselovskii, I., and Zamorano, F.: Australian
980 wildfire smoke in the stratosphere: the decay phase in 2020/2021 and impact on ozone depletion, *Atmos. Chem.
Phys.*, 22, 7417–7442, 2022, <https://doi.org/10.5194/acp-22-7417-2022>.
- Ohneiser, K., Ansmann, A., Witthuhn, A., Deneke, H., Chudnovsky, A., Walter, G., and Senf, F.: Self-lofting of
wildfire smoke in the troposphere and stratosphere: simulations and space lidar observations, *Atmos. Chem.
Phys.*, 23, 2901–2925, 2023, <https://doi.org/10.5194/acp-23-2901-2023>.
- 985 Osborn, M. T., DeCoursey, R. J., Trepte, C. R., Winker, D. M., and Woods, D. C.: Evolution of the Pinatubo
volcanic cloud over Hampton, Virginia, *Geophys. Res. Lett.*, 22, 1101–1104, 1995.
- Owens, J. C.: Optical refractive index of air: dependence on pressure, temperature and composition, *Appl. Opt.*,
6, 51-59, 1967.
- Peterson, D. A., Campbell, J. R., Hyer, E. J., Fromm, M. D., Kablick III, G. P., Cossuth, J. H., and DeLand, M.
990 T.: Wildfire-driven thunderstorms cause a volcano-like stratospheric injection of smoke, *Nature Partner Journals,
Climate and Atmospheric Science*, 8 pp., 1:30, doi:10.1038/s41612-018-0039-3, 2018.
- Peterson, D. A., Fromm, M. D., McRae, R. H. D., Campbell, J. R., Hyer, E. J., Taha, G., Camacho, C. P.,
Kablick III, G. P., Schmidt, C. C., and DeLand, M. T.: Australia’s Black Summer pyrocumulonimbus super
outbreak reveals potential for increasingly extreme stratospheric smoke events, *npj Climate and Atmospheric
995 Science*, 4:38, <https://doi.org/10.1038/s41612-021-00192-9>, 16 pp., 2021.
- Petzold, A., Weinzierl, B., Huntrieser, H., Stohl, A., Real, E., Cozic, J., Fiebig, M., Hendricks, J., Lauer, A.,
Law, K., Roiger, A., Schlager, H., and Weingartner, E.: Perturbation of the European free troposphere aerosol by
North American forest fire plumes during the ICARTT-ITOP experiment in summer 2004, *Atmos. Chem. Phys.*,
7, 5105–5127, www.atmos-chem-phys.net/7/5105/2007/, 2007.
- 1000 Placzek, G., and Teller, E.: Die Rotationsstruktur der Raman-Banden mehratomiger Moleküle, *Z. Phys.*, 81, 209-
258, 1933.
- Proud, S. R., Prata, A. T., and Schmauß, S.: The January 2022 eruption of Hunga Tonga-Hunga Ha’apai volcano
reached the mesosphere, *Science*, 378, 554-557, 2022.
- Reichardt, J., and Reichardt, S.: Determination of cloud effective particle size from the multiple-scattering effect
1005 on lidar integration-method temperature measurements, *Appl. Opt.*, 45, 2796-2804.
- Reiter, R., and Carnuth, W.: Comparing Lidar Reflectivity Profiles Against Measured Profiles of Vertical
Aerosol Distribution between 1 and 3 km a.s.l., *Arch. Met. Geophys. Biokl. A* 24, 69-92, 1975.
- Reiter, R., Jäger, H., Carnuth, W., and Funk, W.: The Stratospheric Aerosol Layer Observed by Lidar Since
October 1976. A Contribution to the Problem of Hemispheric Climate, *Arch. Met. Geophys. Biokl. B*, 27, 121-
1010 149, 1979.

- Schoeberl, M. R., Wang, Y., Ueyama, R., Taha, G., Jensen, E., and Yu, W.: Analysis and Impact of the Hunga Tonga-Hunga Ha'apai Stratospheric Water Vapor Plume, *Geophys. Res. Lett.*, 49, e2022GL100248. <https://doi.org/10.1029/2022GL100248>, 8 pp., 2022.
- 1015 Simonich, D. M., and Clemesha, B. R.: A history of aerosol measurements at São José dos Campos, Brazil (23 S, 46 W) from 1972 to 1995. *Advances in Atmospheric Remote Sensing with Lidar — Selected Papers of the 18th International Laser Radar Conference (Berlin, Germany, 1996)*, A. Ansmann, R. Neuber, P. Rairoux, U. Wandinger, Eds., Springer (Berlin, Heidelberg, New York), 379-382, 1997.
- Solomon, S., Daniel, J. S., Neely III, R. R., Vernier, J.-P., Dutton, E. G., and Thomason, L. W.: The Persistently Variable "Background" Stratospheric Aerosol Layer and Global Climate Change, *Science*, 333, 866-870, 2011.
- 1020 Speidel, J., and Vogelmann, H.: Correct(ed) Klett-Fernald algorithm for elastic aerosol backscatter retrievals: A sensitivity analysis, *Appl. Opt.*, 62, 861-868, 2023.
- Sprenger, M., and Wernli, H.: A northern hemispheric climatology of cross-tropopause exchange for the ERA15 time period (1979–1993), *J. Geophys. Res.*, 108, 8521 doi: 10.1029/2002JD002636, STA 6, 14 pp., 2003.
- 1025 Stein, A. F., Draxler, R. R., Rolph, G. D., Stunder, B. J. B., Cohen, M. D., and Ngan, F.: NOAA's HYSPLIT atmospheric transport and dispersion modeling system, *B. Am. Meteorol. Soc.*, 96, 2059–2077, 2015.
- Steinbrecht, W., Claude, H., Schönenborn, F., Leiterer, U., Dier, H., and Lanzinger, E.: Pressure and Temperature Differences between Vaisala RS80 and RS92 Radiosonde Systems, *J. Atmos. Oceanic Technol.*, 25, 909-927, 2008.
- 1030 Stenchikov, G., Ukhov, A., Osipov, S., Ahmadov, R., Grell, G., Cady-Pereira, K., Mlawer, E., and Iacono, M.: How Does a Pinatubo-Size Volcanic Cloud Reach the Middle Stratosphere? *J. Geophys. Res.*, 126, e2020JD033829. <https://doi.org/10.1029/2020JD033829>, 33 pp., 2021.
- Solomon, S., Portmann, R. W., Garcia, R., Thomason, L. W., Poole, L. R., and McCormick, M. P.: The role of aerosol variations in anthropogenic ozone depletion at northern midlatitudes, *J. Geophys. Res.*, 101, 6713-6727, 1996.
- 1035 Stohl, A.: A 1-year Lagrangian "climatology" of airstreams in the Northern Hemisphere troposphere and lowermost stratosphere, *J. Geophys. Res.*, 106, 7263-7279, 2001.
- Stohl, A. and Trickl, T.: A textbook example of long-range transport: Simultaneous observation of ozone maxima of stratospheric and North American origin in the free troposphere over Europe, *J. Geophys. Res.*, 104, 30445-30462, 1999.
- 1040 Stohl, A., Bonasoni, P., Cristofanelli, P., Collins, W., Feichter, J., Frank, A., Forster, C., Gerasopoulos, E., Gäggeler, H., James, P., Kentarchos, T., Kromp-Kolb, H., Krüger, B., Land, C., Meloen, J., Papayannis, A., Priller, A., Seibert, P., Sprenger, M., Roelofs, G. J., Scheel, H. E., Schnabel, C., Siegmund, P., Tobler, L., Trickl, Sprenger, M., Croci Maspoli, M., and Wernli, H.: Tropopause folds and cross-tropopause exchange: A global investigation based upon ECMWF analyses for the time period March 2000 to February 2001, *J. Geophys. Res.*, 108, 8518, doi: 10.1029/2002JD002587, STA 3, 11 pp., 2003.
- 1045 Taha, G., Loughman, R., Colarco, P. R., Zhu, T., Thomason, L. W., and Jaross, G.: Tracking the 2022 Hunga Tonga-Hunga Ha'apai Aerosol Cloud in the Upper and Middle Stratosphere Using Space-Based Observations,

- Geophys. Res. Lett., 49, e2022GL100091. <https://doi.org/10.1029/2022GL100091>, 9 pp. and 11 pp. of supporting information, 2022.
- 1050 Teitelbaum, H., Moustououi, M., and Fromm, M.: Exploring polar stratospheric cloud and ozone minhole formation: The primary importance of synoptic-scale flow perturbations, *J. Geophys. Res.*, 106, 28173-28188, 2001.
- Thomason, L. W., Poole, L. R., and Deshler, T.: A global climatology of stratospheric aerosol surface area density deduced from stratospheric aerosol and gas experiment II measurements: 1984–1994. *J. Geophys. Res.*
- 1055 102, 8967–8976, 1997.
- Thomason, L. W., and Peter, T.: Assessment of stratospheric aerosol properties (WCRP-124, WMO/TD-1295, SPARC Report 4). Retrieved from <https://www.sparc-climate.org/data-centre/data-access/assessment-of-stratospheric-aerosol-properties/>, 2006.
- Thomason, L. W., and Bedka, K. M.: Increase in upper tropospheric and lower stratospheric aerosol levels and
- 1060 its potential connection with Asian pollution, *J. Geophys. Res.*, 120, 1608–1619, doi:10.1002/2014JD022372, 2015.
- Thomason, L. W., Ernest, N., Millán, L., Rieger, L., Bourassa, A., Vernier, J.-P., Manney, G., Luo, B., Arfeuille, F., and Peter, T.: A global space-based stratospheric aerosol climatology: 1979–2016, *Earth Syst. Sci. Data*, 10, 469–492, <https://doi.org/10.5194/essd-10-469-2018>, 2018.
- 1065 Thomason, L. W., Kovilakam, M., Schmidt, A., Savigny, C., Knepp, T., and Rieger, L.: Evidence for the predictability of changes in the stratospheric aerosol size following volcanic eruptions of diverse magnitudes using space-based instruments, *Atmos. Chem. Phys.*, 21, 1143–1158, 2021, <https://doi.org/10.5194/acp-21-1143-2021>.
- Torres, O., Bhartia, P. K., Taha, G., Jethva, H., Das, S., Colarco, P., Krotkov, N., Omar, A., and Ahn, C.:
- 1070 Stratospheric Injection of Massive Smoke Plume From Canadian Boreal Fires in 2017 as Seen by DSCOVR-EPIC, CALIOP, and OMPS-LP Observations, *J. Geophys. Res.*, 125, e2020JD032579. <https://doi.org/10.1029/2020JD032579>, 25 pp., 2020.
- Trepte, C. R., and Hitchman, M. H.; Tropical stratospheric circulation deduced from satellite aerosol data, *Nature*, 355, 626-628, 1992.
- 1075 Trickl, T.: Summary on Rayleigh and Rotational Raman Scattering for the ISSI Team of the NDACC Lidar Working Group, <http://www.trickl.de/Rayleigh.pdf>, 14 pp., 2023.
- Trickl, T., Proch, D., and Kompa, K. L.: Resonance-Enhanced 2 + 2 Photon Ionization of Nitrogen: The Lyman-Birge-Hopfield Band System, *J. Mol. Spectrosc.*, 162, 184-229, 1993.
- Trickl, T., Proch, D., and Kompa, K. L.: The Lyman-Birge-Hopfield System of Nitrogen: Revised Calculation of
- 1080 the Energy Levels, *J. Mol. Spectrosc.*, 171, 374-384, 1995.
- Trickl, T., Cooper, O. R., Eisele, H., James, P., Mücke, R., and Stohl, A.: Intercontinental transport and its influence on the ozone concentrations over central Europe: Three case studies. *J. Geophys. Res.*, 108, 8530, doi:10.1029/2002JD002735, *STA* 15, 23 pp., 2003.

- 1085 Trickl, T., Feldmann, H., Kanter, H.-J., Scheel, H. E., Sprenger, M., Stohl, A., and Wernli, H.: Deep stratospheric intrusions over Central Europe: case studies and climatological aspects, *Atmos. Chem. Phys.*, 10, 499-524, 2010.
- Trickl, T., Eisele, H., Bärtsch-Ritter, N. Furger, M., Mücke, R., Sprenger, M., and Stohl, A.: High-ozone layers in the middle and upper troposphere above Central Europe: Potential ozone import from the stratosphere along the subtropical jet stream, *Atmos. Chem. Phys.*, 11, 9343-9366, 2011.
- 1090 Trickl, T., Giehl, H., Jäger, H., and Vogelmann, H.: 35 years of stratospheric aerosol measurements at Garmisch-Partenkirchen: from Fuego to Eyjafjallajökull, and beyond, *Atmos. Chem. Phys.*, 13, 5205-5225, 2013.
- Trickl, T., Vogelmann, H., Giehl, H., Scheel, H.-E., Sprenger, M., and Stohl, A.: How stratospheric are deep stratospheric intrusions?, *Atmos. Chem. Phys.*, 14, 9941–9961, 2014, <https://doi.org/10.5194/acp-14-9941-2014>.
- 1095 Trickl, T., Vogelmann, H., Flentje, H., and Ries, L.: Stratospheric ozone in boreal fire plumes – the 2013 smoke season over Central Europe, *Atmos. Chem. Phys.*, 15, 9631-9649, 2015, <https://doi.org/10.5194/acp-15-9631-2015>.
- Trickl, T., Vogelmann, H., Fix, A., Schäfler, A., Wirth, M., Calpini, B., Levrat, G., Romanens, G., Apituley, A., Wilson, K. M., Begbie, R., Reichardt, J., Vömel, H. and Sprenger, M.: How stratospheric are deep stratospheric intrusions into the troposphere? LUAMI 2008, *Atmos. Chem. Phys.*, 16, 8791-8815, 2016, <https://doi.org/10.5194/acp-16-8791-2016>.
- 1100 Trickl, T., Giehl, H., Neidl, F., Perfahl, M., and Vogelmann, H.: Three decades of tropospheric ozone lidar development at Garmisch-Partenkirchen, Germany, *Atmos. Meas. Tech.*, 13, 6357–6390, 2020a.
- Trickl, T., Vogelmann, H., Ries, L., and Sprenger, M.: Very high stratospheric influence observed in the free troposphere over the Northern Alps – just a local phenomenon? *Atmos. Chem. Phys.*, 20, 243-266, 2020b.
- 1105 Trickl, T., Adelwart, M., Khordakova, D., Ries, L., Rolf, C., Steinbrecht, W., and Vogelmann, H.: Local comparisons of tropospheric ozone: Vertical soundings at two neighbouring stations in Southern Bavaria, *Atmos. Meas. Tech.*, 16, 5145–5165, 2023, <https://doi.org/10.5194/amt-16-5145-2023>.
- Vernier, J.-P., Thomason, and Kar, J.: CALIPSO detection of an Asian tropopause aerosol layer, *Geophys. Res. Lett.*, 38, L07804, doi: 10.1029/2010GL046614, 6 pp., 2011a.
- 1110 Vernier, J.-P., Thomason, L. W., Pommereau, J.-P., Bourassa, A., Pelon, J., Garnier, A., Hauchecorne, A., Blanot, L. Trepte, C., Degenstein, D., and Vargas, F.: Major influence of tropical volcanic eruptions on the stratospheric aerosol layer during the last decade, *Geophys. Res. Lett.*, 38, L12807, doi: 10.1029/2011GL047563, 8 pp., 2011b.
- Vernier, J.-P., Pommereau, J.-P., Thomason, L. W., Pelon, J., Garnier, A., Deshler, T., Jumelet, J., and Nielsen, J. K.: Overshooting of clean tropospheric air in the tropical lower stratosphere as seen by the CALIPSO lidar, *Atmos. Chem. Phys.*, 11, 9683–9696, 2011; doi:10.5194/acp-11-9683-2011.
- 1115 Vernier, J.-P., Barnes, J. E., Thomason, L. W., Keckhut, P., Jumelet, J., David-Beausire, C., Trickl, T., Giehl, H., Liley, J. B., and T. Nagai: Do lidar systems have enough sensitivity to detect annual cycling in stratospheric aerosol scattering ratio? Unpublished manuscript, 38 pp., 2013; available from the authors.
- Vernier, J.-P., Fairlie, T. D., Natarajan, M., Wienhold, F. G., Bian, J., Martinsson, B. G., Crumeyrolle, S., T.,
1120 Thomason, L.W., and K. M. Bedka, K. M.: Increase in upper tropospheric and lower stratospheric aerosol levels

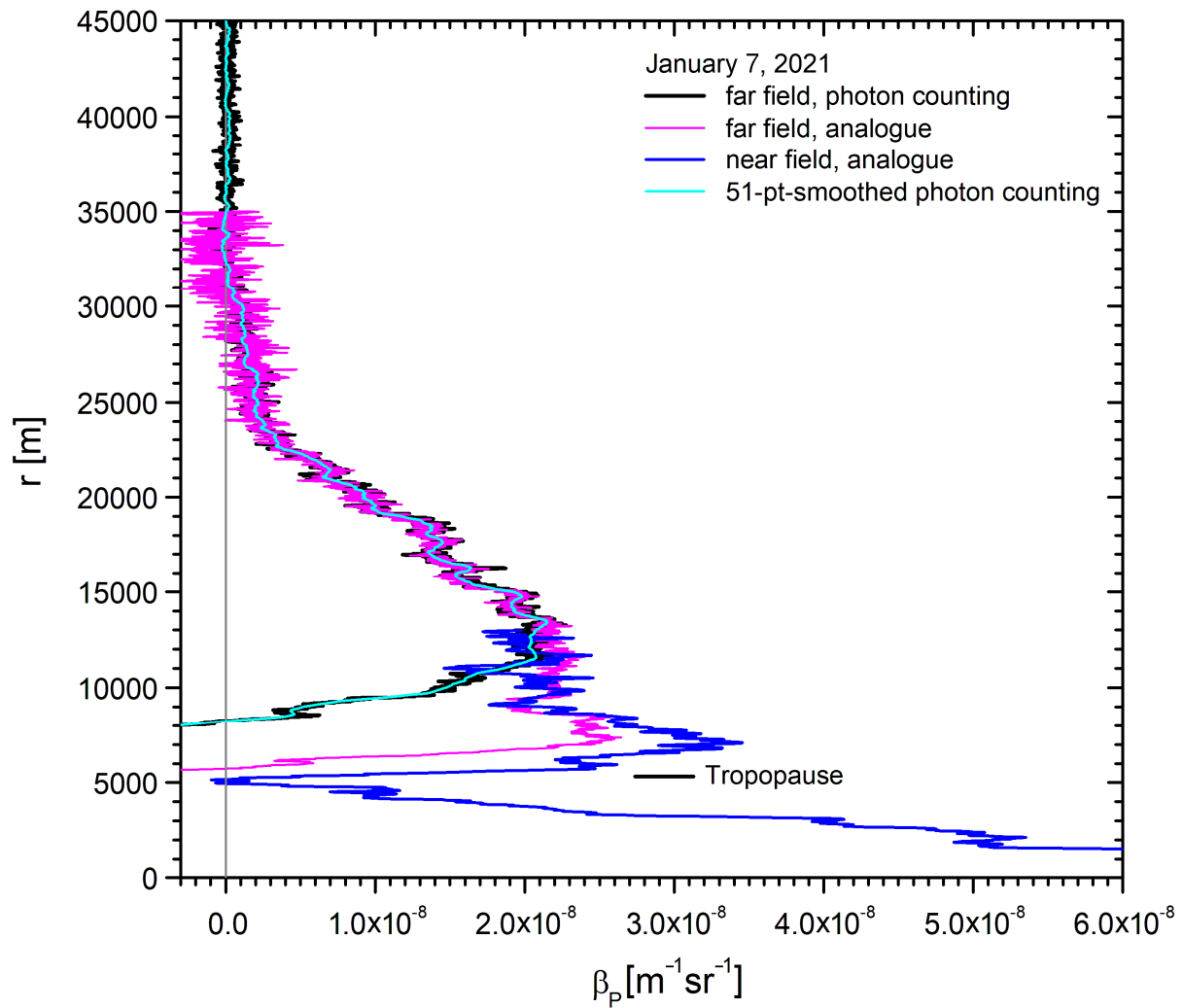
- and its potential connection with Asian pollution, *J. Geophys. Res.*, 120, 1608–1619, doi:10.1002/2014JD022372, 2015.
- Vernier, J. P., Fairlie, T. D., Deshler, T., Natarajan, M., Knepp, T., Foster, K., Wienhold, F. G., Bedka, K. M., Thomason, L., and Trepte, C.: In situ and space-based observations of the Kelud volcanic plume: The persistence of ash in the lower stratosphere, *J. Geophys. Res.*, 121, 11104–11118, <https://doi.org/10.1002/2016jd025344>, 2016.
- Vömel, H., Evan, S., and Tully, M.: Water vapor injection into the stratosphere by Hunga Tonga-Hunga Ha’apai, *Science*, 377, 1444-1447, 2022.
- Vogelmann, H. and Trickl, T.: Wide-range sounding of free-tropospheric water vapor with a differential-absorption lidar (DIAL) at a high-altitude station, *Appl. Opt.*, 47, 2116-2132, 2008.
- 1130 Wernli, H., and Bourqui, M.: A Lagrangian “1-year climatology” of (deep) cross-tropopause exchange in the extratropical Northern Hemisphere, *J. Geophys. Res.*, 107, 4021, 10.1029/2001JD000812, *ACL* 13, 16 pp., 2002.
- Winker, D. M., and Osborn, M. T.: Airborne lidar observations of the Pinatubo volcanic plume, *Geophys. Res. Lett.*, 19, 167–170. <https://doi.org/10.1029/91gl02867>, 1992.
- WMO: Atmospheric Ozone 1985 Assessment of our Understanding of the Processes Controlling its Present Distribution and Change, Report No. 16, Vol. I, World Meteorological Organization, Geneva (Switzerland), 264 pp., 1986.
- 1135
- Zhu, Y., Toon, O. B., Lambert, A., Kinnison, D. E., Brakebusch, M., Bardeen, C. G., Mills, M. J., and English, J. M.: Development of a Polar Stratospheric Cloud Model within the Community Earth System Model using constraints on Type I PSCs from the 2010–2011 Arctic winter, *Journal of Advances in Modeling Earth Systems*, 7, 551–585, <https://doi.org/https://doi.org/10.1002/2015MS000427>, 2015.
- 1140
- Zanis, P., Trickl, T., Stohl, A., Wernli, H., Cooper, O., Zerefos, C., Gaeggeler, H., Priller, A., Schnabel, C., Scheel, H. E., Kanter, H. J., Tobler, L., Kubik, P. W., Cristofanelli, P., Forster, C., James, P., Gerasopoulos, E., Delcloo, A., Papayannis, A., and Claude, H.: Forecast, observation and modelling of a deep stratospheric intrusion event over Europe, *Atmos. Chem. Phys.*, 3, 763-777, 2003.
- 1145
- Xu, J., Li, D., Bai, Z., Tao, M., and Bian, J.: Large Amounts of Water Vapor Were Injected into the Stratosphere by the Hunga Tonga–Hunga Ha’apai Volcano Eruption, *Atmosphere*, 13, 912. <https://doi.org/10.3390/atmos13060912>, 9 pp., 2022.
- Zuev, V. V., Burlakov, V. D., Nevzorov, A. V., Pravdin, V. L., Savelieva, E. S., and Gerasimov, V. V.: 30-year lidar observations of the stratospheric aerosol layer state over Tomsk (Western Siberia, Russia), *Atmos. Chem. Phys.* 17, 3067–3081, <https://doi.org/10.5194/acp-17-3067-2017>, 2017.
- 1150
- Zuev, V. V., Gerasimov, V. V., Nevzorov, A. V., and Savelieva, E. S., Lidar observations of pyrocumulonimbus smoke plumes in the UTLS over Tomsk (Western Siberia, Russia) from 2000 to 2017, *Atmos. Chem. Phys.*, 19, 3341–3356, <https://doi.org/10.5194/acp-19-3341-2019>, 2019.
- Zhu, Y., Toon, O. B., Kinnison, D., Harvey, V. L., Mills, M. J., Bardeen, C. G., Pitts, M., Bègue, N., Renard, J.-B., Berthet, G., and Jégou, F.: Stratospheric Aerosols, Polar Stratospheric Clouds, and Polar Ozone Depletion After the Mount Calbuco Eruption in 2015, *Journal of Geophysical Research: Atmospheres*, 123, 12308–12331, <https://doi.org/https://doi.org/10.1029/2018JD028974>, 2018.
- 1155

1160 **Table 1.** Some operating conditions of the new lidar system

<i>Period</i>	<i>number of laser shots</i>	<i>detection mode</i>
2016 – Sept. 2017	10000	analogue
Oct. 2017 – 19 Feb. 2018	20000	analogue
25 Feb. 2018 – Apr. 2018	50000	analogue; April: photon counting
1165 May and June 2018	20000	analogue and (June) photon counting
July 2018 – Aug. 2019	40000	analogue and photon counting
Sept. 2019	100000	analogue (failure of the counting system)
Oct. 2019 – June 2020	40000	analogue and photon counting
Since July 2020	100000	analogue and photon counting

1170

Figures:



1175 **Fig. 1.** Backscatter coefficients from the Klett inversions of the data of the near- and far field detection channels in the evening of 7 January 2021 (100000 laser shots); the values are displayed with bin sizes of 7.5 m (old system: 75 m, same noise amplitude up to 40 km). The photon-counting values are smoothed with a ± 25 -bin sliding average that reveals the high far-field performance of the system. Please, note the low wintertime Munich tropopause at $r = 5.3$ km ($h = 8.0$ km). $r = 0$ m corresponds to 2675 m a.s.l. (laboratory at UFS). The aerosol below 5 km was advected from Ukraine and Turkey.

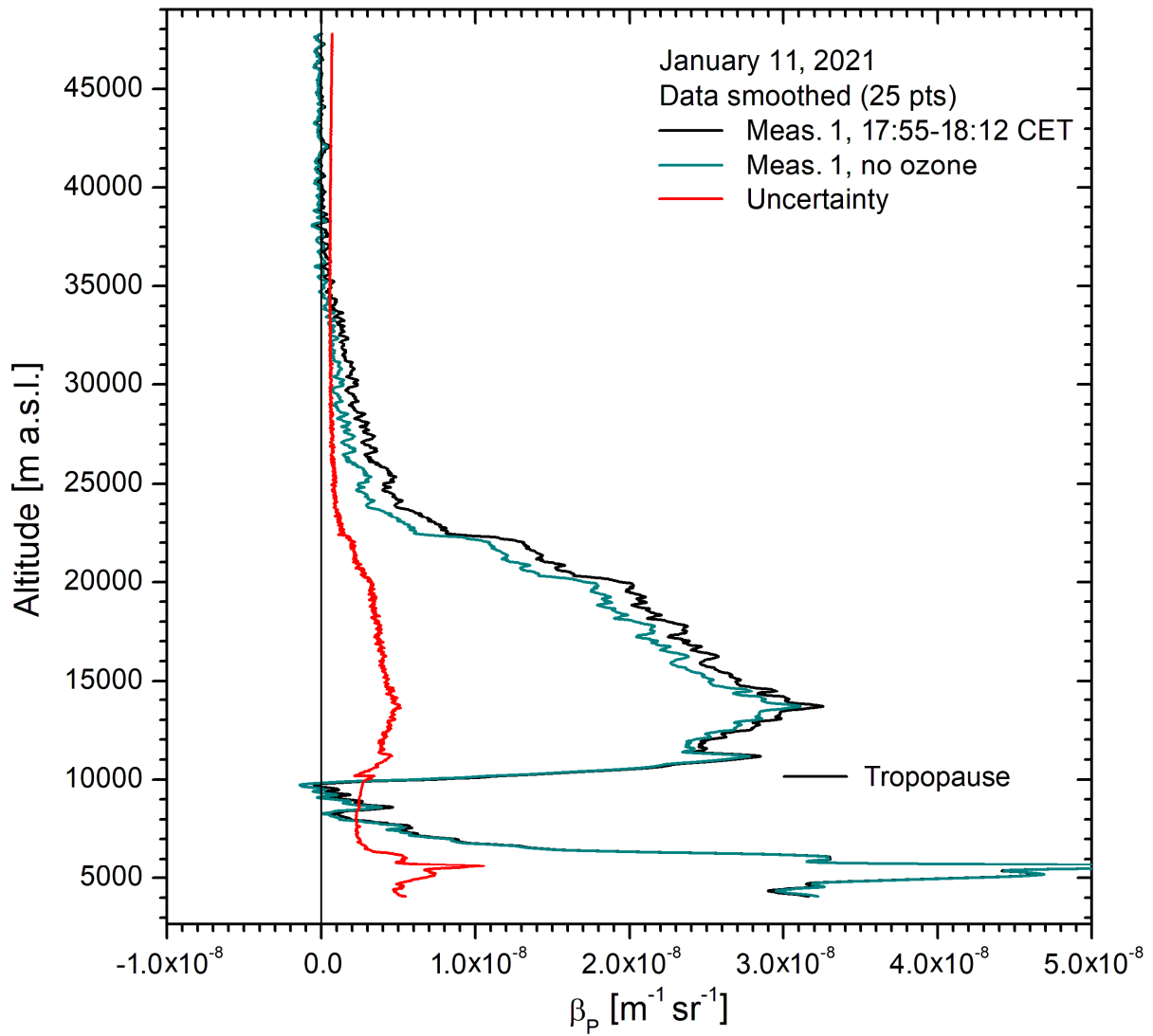
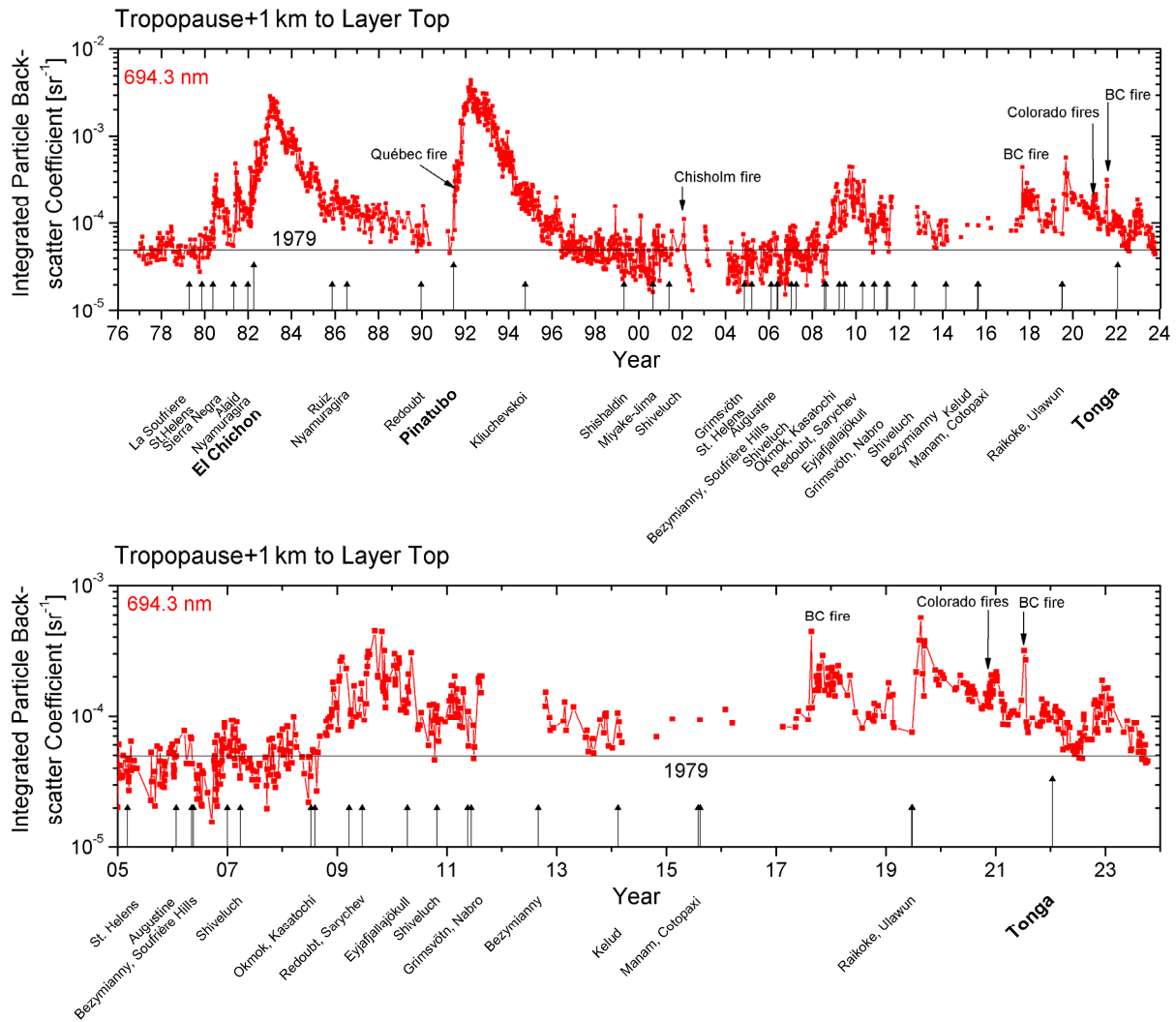


Fig. 2. Comparison of the retrievals with (black curve) and without (blue curve) ozone correction (11 January, 2021); the data were smoothed with a running arithmetic average over ± 12 bins (± 90 m).



1185 **Fig. 3.** Upper panel: Time series of the integrated stratospheric backscatter coefficient from the lidar measurements at Garmisch-Partenkirchen: The backscatter coefficients are integrated from 1 km above the tropopause to the upper end of the layer.

Lower panel: Section of the upper panel from 2005 to 2021

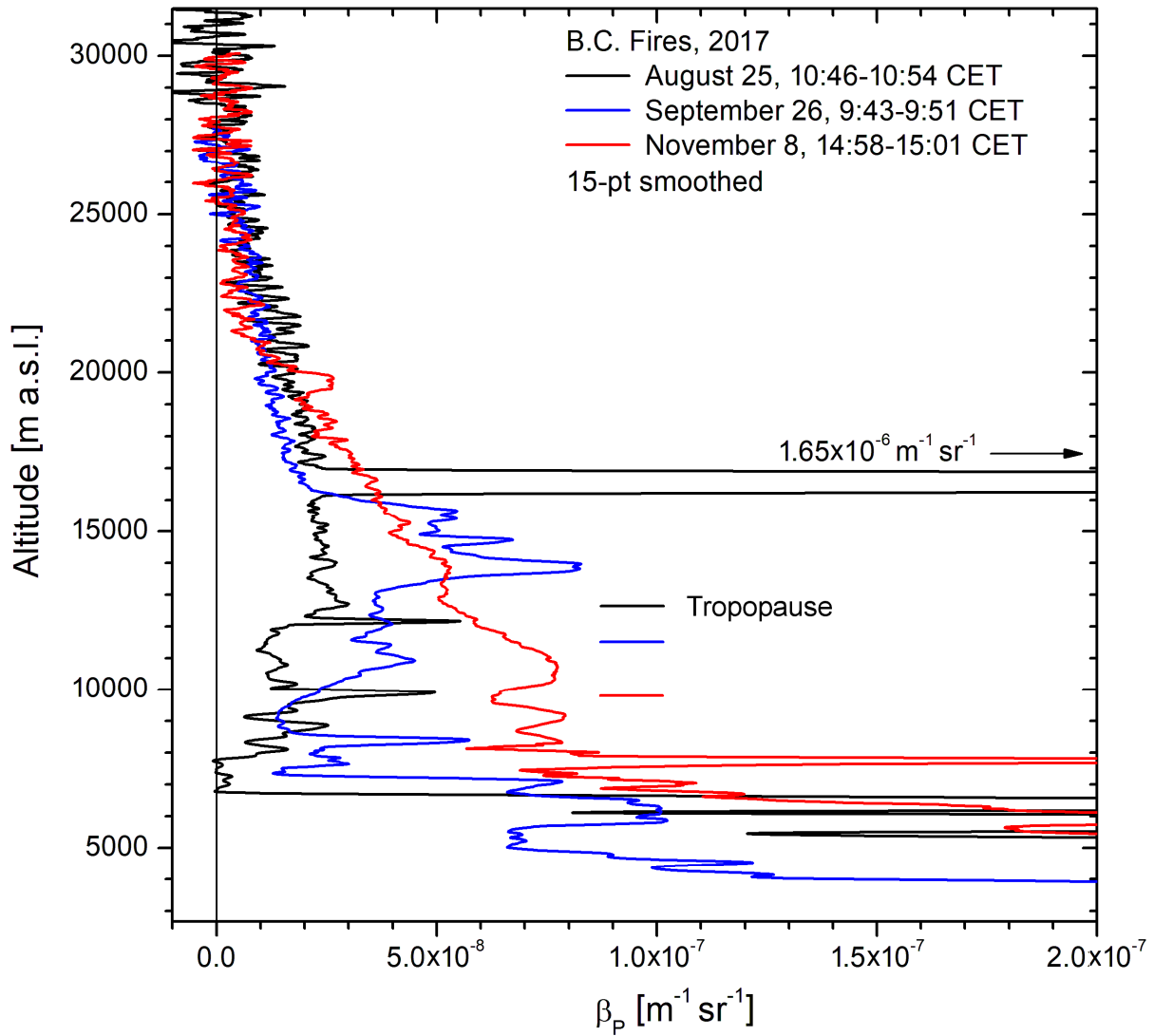
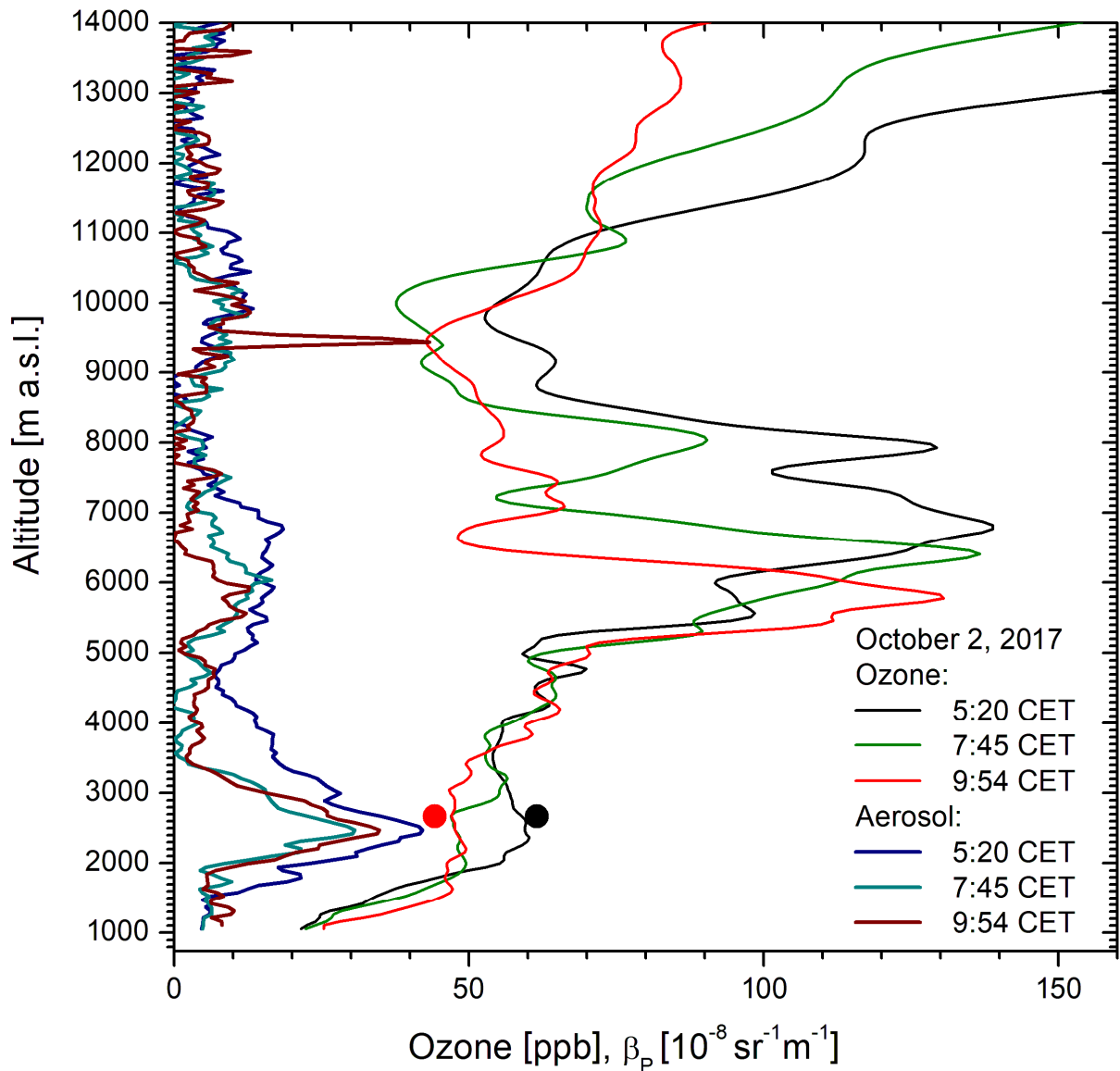
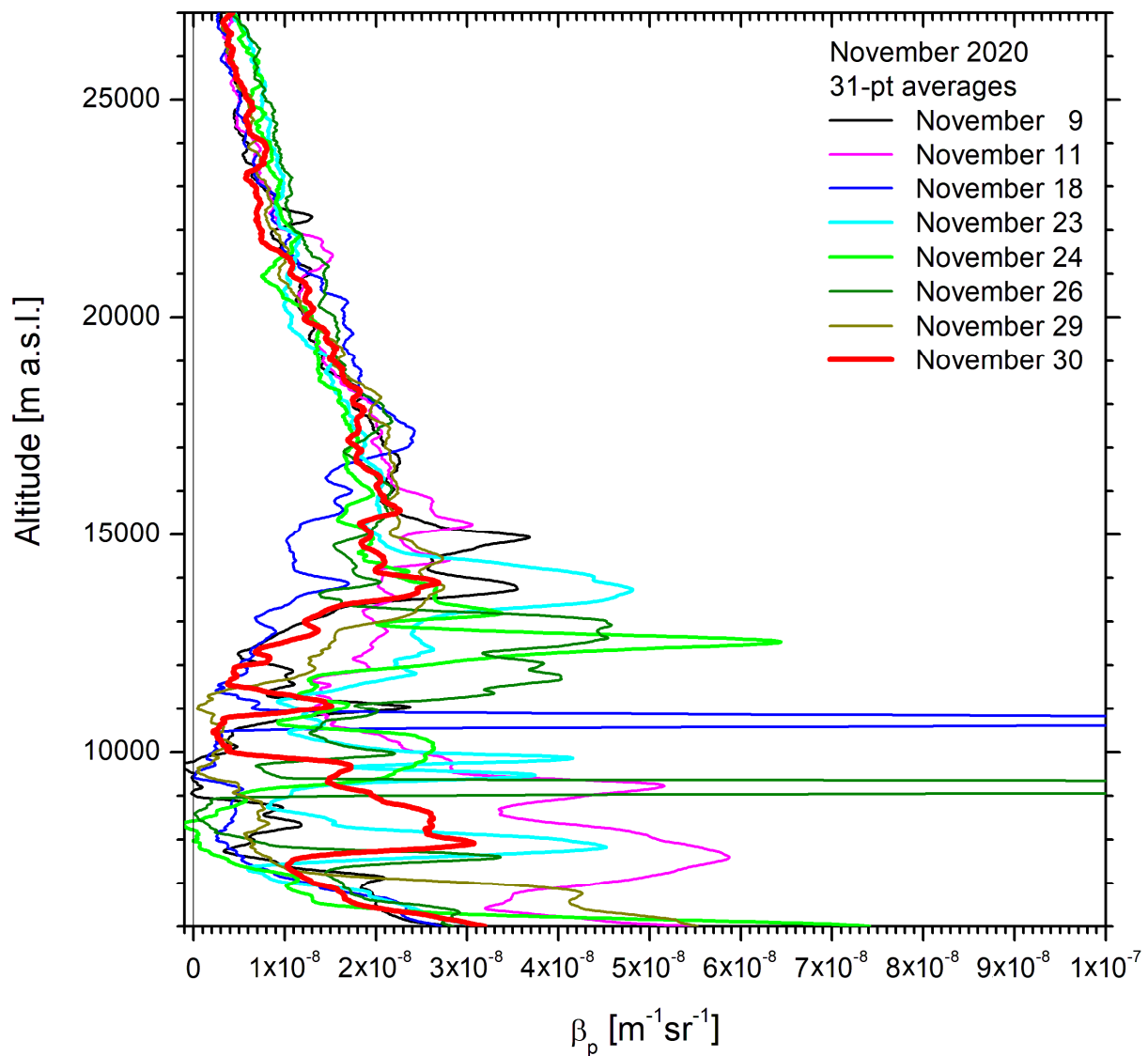


Fig. 4. Three examples of 532-nm backscatter coefficients following the British Columbia (B.C.) fires in 2017; the data are slightly smoothed (sliding arithmetic average over ± 7 bins) because of elevated noise due to analogue data acquisition, daytime conditions and just 20000 laser shots. The corrected tropopause altitudes from the Munich radiosonde are marked in the colours of the corresponding backscatter coefficients.



1200 **Fig. 6.** Ozone mixing ratios and 313-nm aerosol backscatter coefficients derived from measurements of the
 ozone DIAL at IMK-IFU on 2 October 2017, showing aerosol in a descending intrusion layer giving rise to a
 313-nm aerosol backscatter coefficient of almost $2 \times 10^{-7} \text{ m}^{-1} \text{ sr}^{-1}$ between roughly 5 and 7 km. The aerosol spike
 at 9.45 km could be a weak cirrus and mark the upper end of the troposphere. For comparison we also give the
 ozone mixing ratios measured at UFS at 5:30 and 10:00 CET (filled circles).

1205



1210 **Fig. 7.** 532-nm aerosol backscatter coefficients from the night-time measurements in November 2020 showing the influence of the fires in Colorado; the two spikes leaving the scale are caused by cirrus clouds. The corrected tropopause altitudes of the Munich radiosonde are 12.65 km, 13.13 km, 12.57 km, 11.41 km, 11.40 km, 10.93 km, 12.34 km and 13.06 km, respectively. See Fig. 1 for the situation after these plumes tapered off.

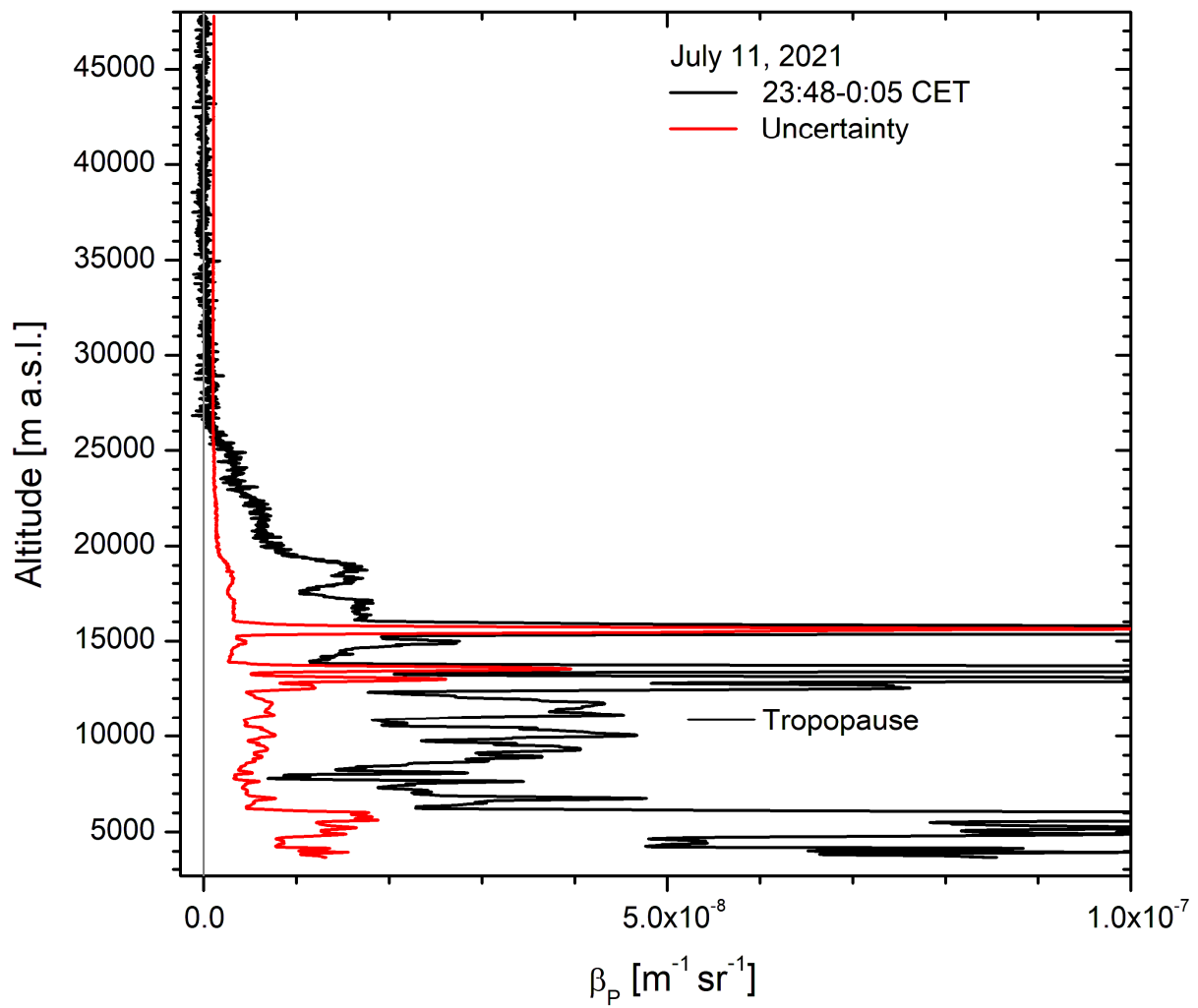


Fig. 8. 532-nm aerosol backscatter coefficients on 11 July 2021; the two maximum values are $2.63 \times 10^{-7} \text{ m}^{-1} \text{ sr}^{-1}$ at 13.5 km and 7.07×10^{-7} at 15.6 km. The relative uncertainty at 15.6 km is estimate as 18 %.

NOAA HYSPLIT MODEL
 Backward trajectories ending at 2300 UTC 11 Jul 21
 GDAS Meteorological Data

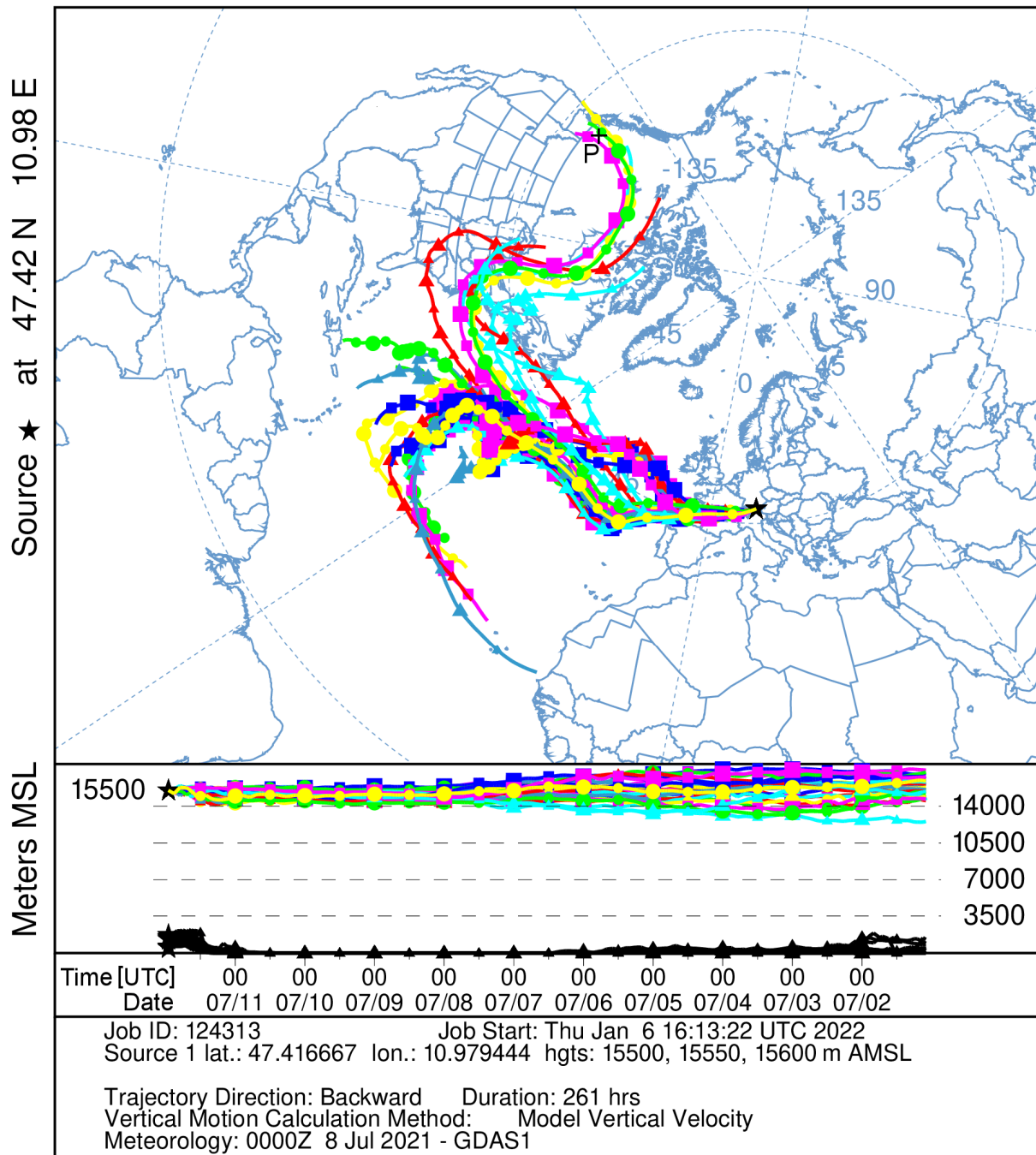


Fig. 9. HYSPLIT ensemble backward trajectories initiated at 15.55 km ± 0.05 km a.s.l. above UFS (Garmisch-Partenkirchen) on 11 July 2021 (23 UTC); the duration of the trajectories is 261 h (see text); the most likely pyro-Cb position at 51.0° N and 120.8° W is marked with a black cross (labelled with P).

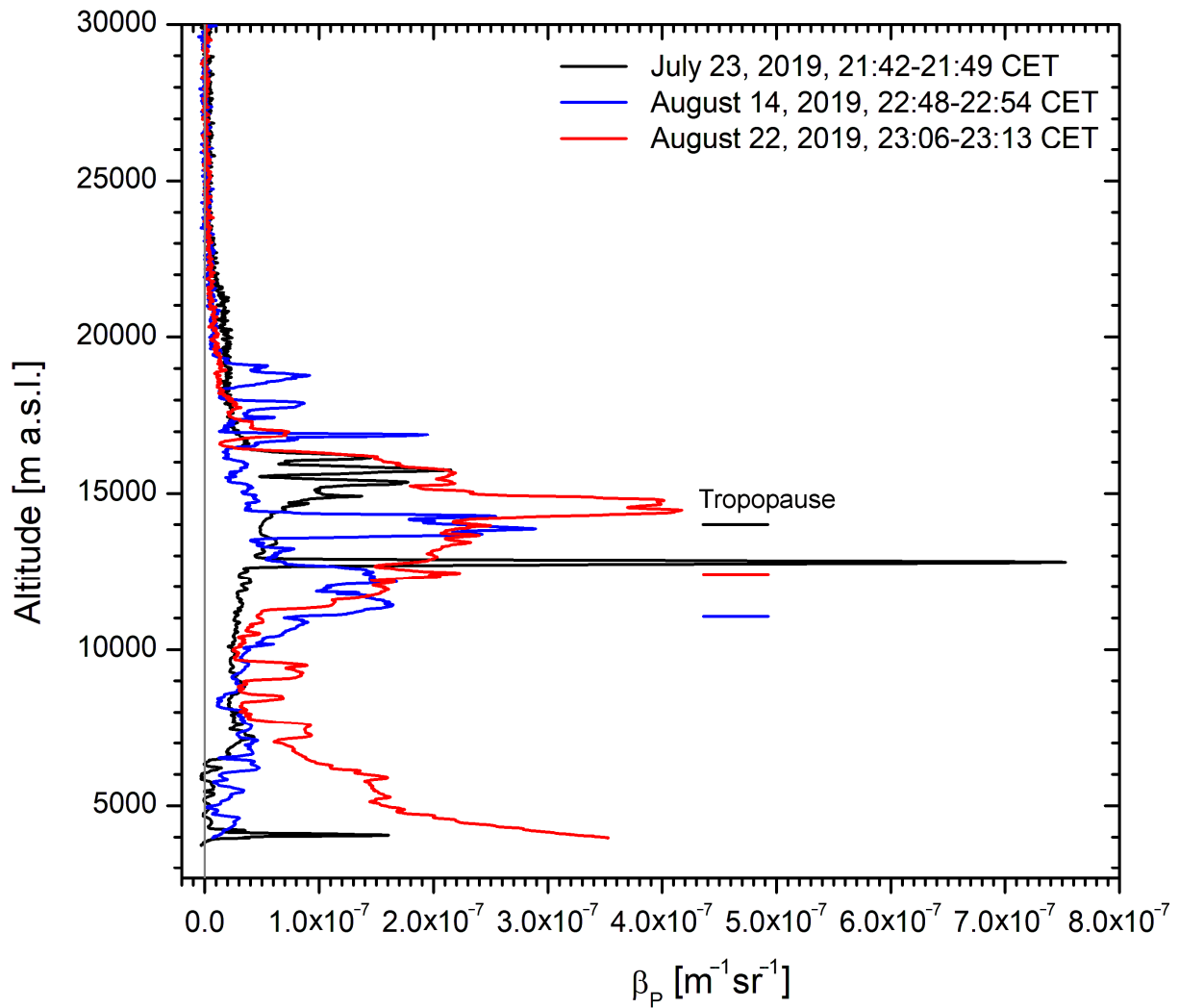
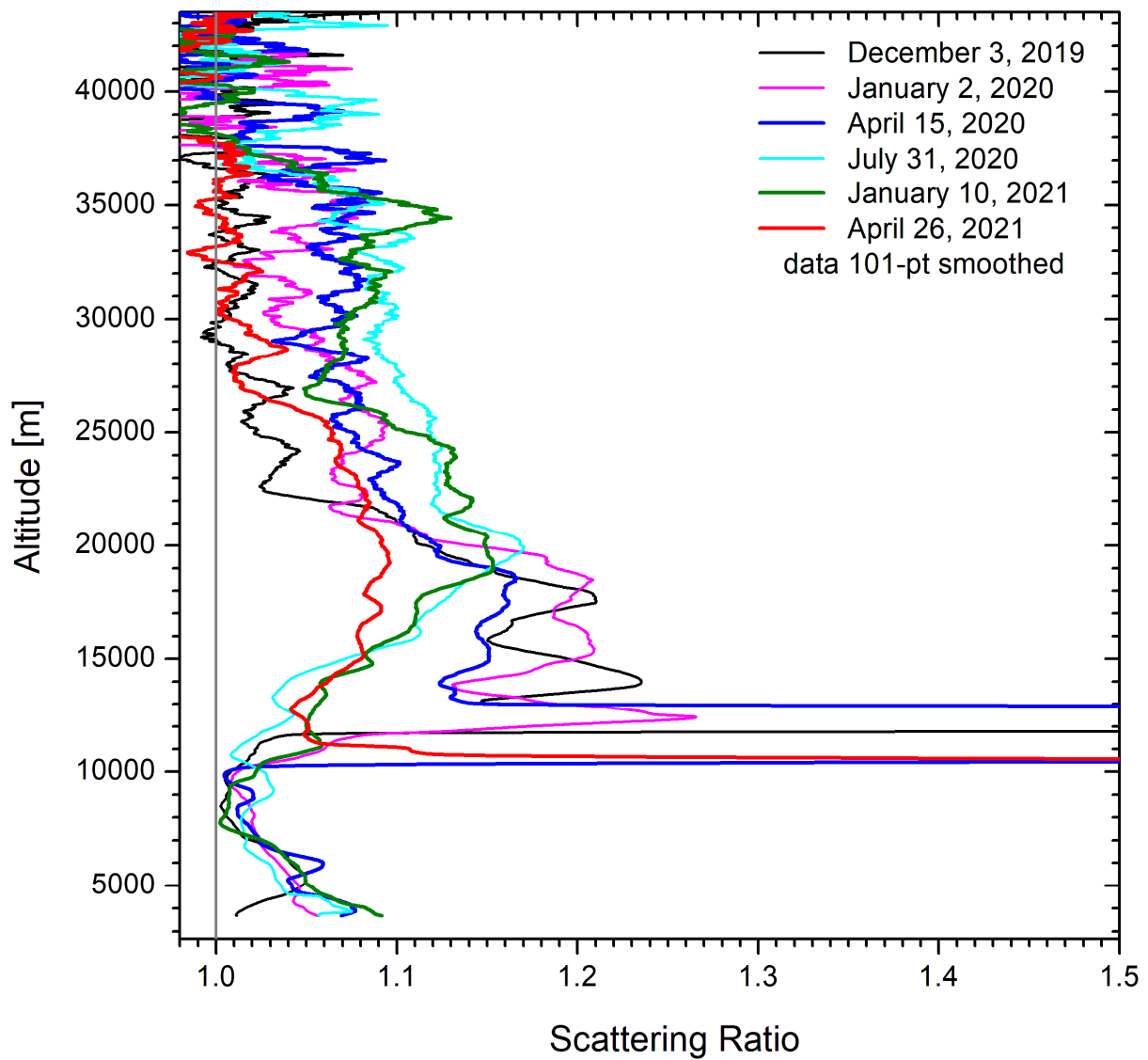


Fig. 10. High 532-nm aerosol backscatter coefficients following the Raikoke volcanic eruption in June 2019; the tropopause levels are 13.89 km, 11.06 km and 12.40 km, respectively. We tend to assume that the spike at 12.8 km on 23 July was caused by a cirrus cloud because it is located below the tropopause. However, the Munich relative humidity at that altitude was less than 30 %. The tropopause altitudes are marked in the colours of the respective backscatter coefficients.



1230 **Fig. 11.** 532-nm scattering ratios smoothed by gliding ± 50 -bin averages for selected measurements in 2019, 2020 and 2021; starting in January 2021 the aerosol layer expanded to more than 28 km a.s.l., possibly caused by northward propagation of the plume from the tropical eruption of Ulawun in the Brewer-Dobson circulation. The uncertainty of the values strongly grows above 35 km because the relative noise in the data starts to exceed the size of the aerosol features.

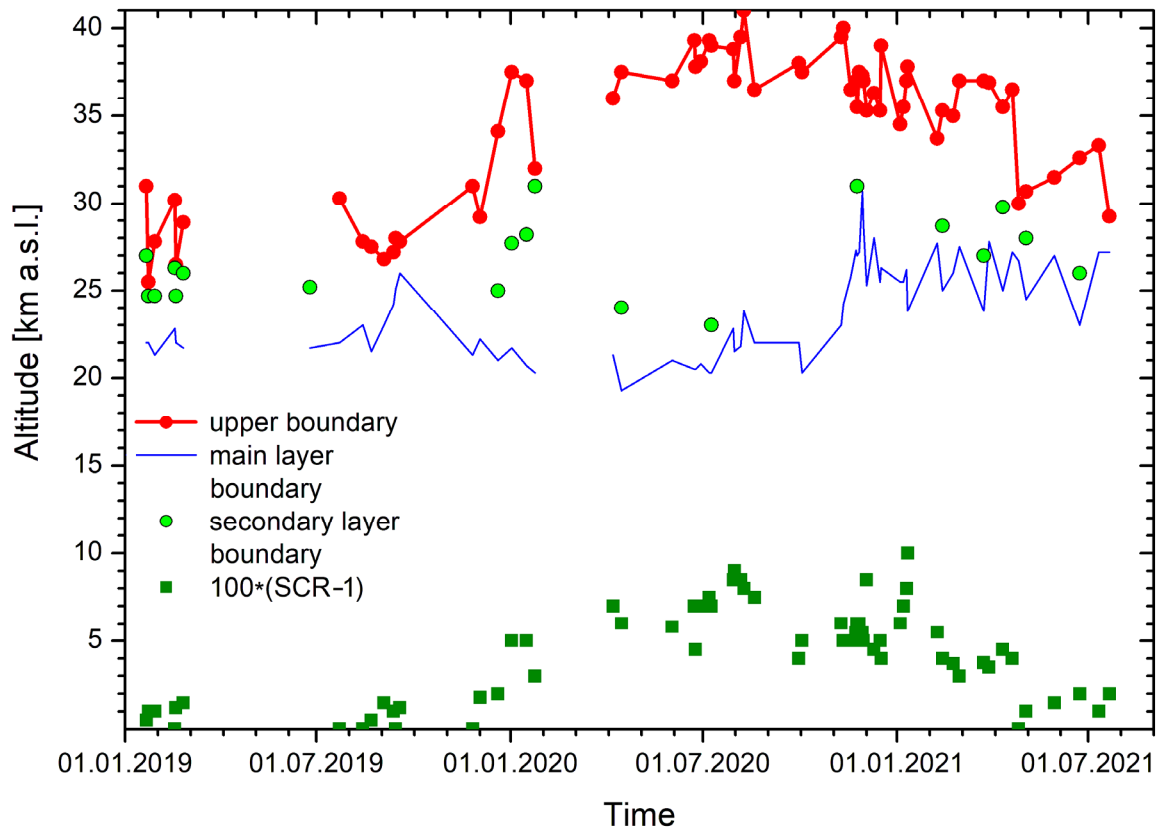
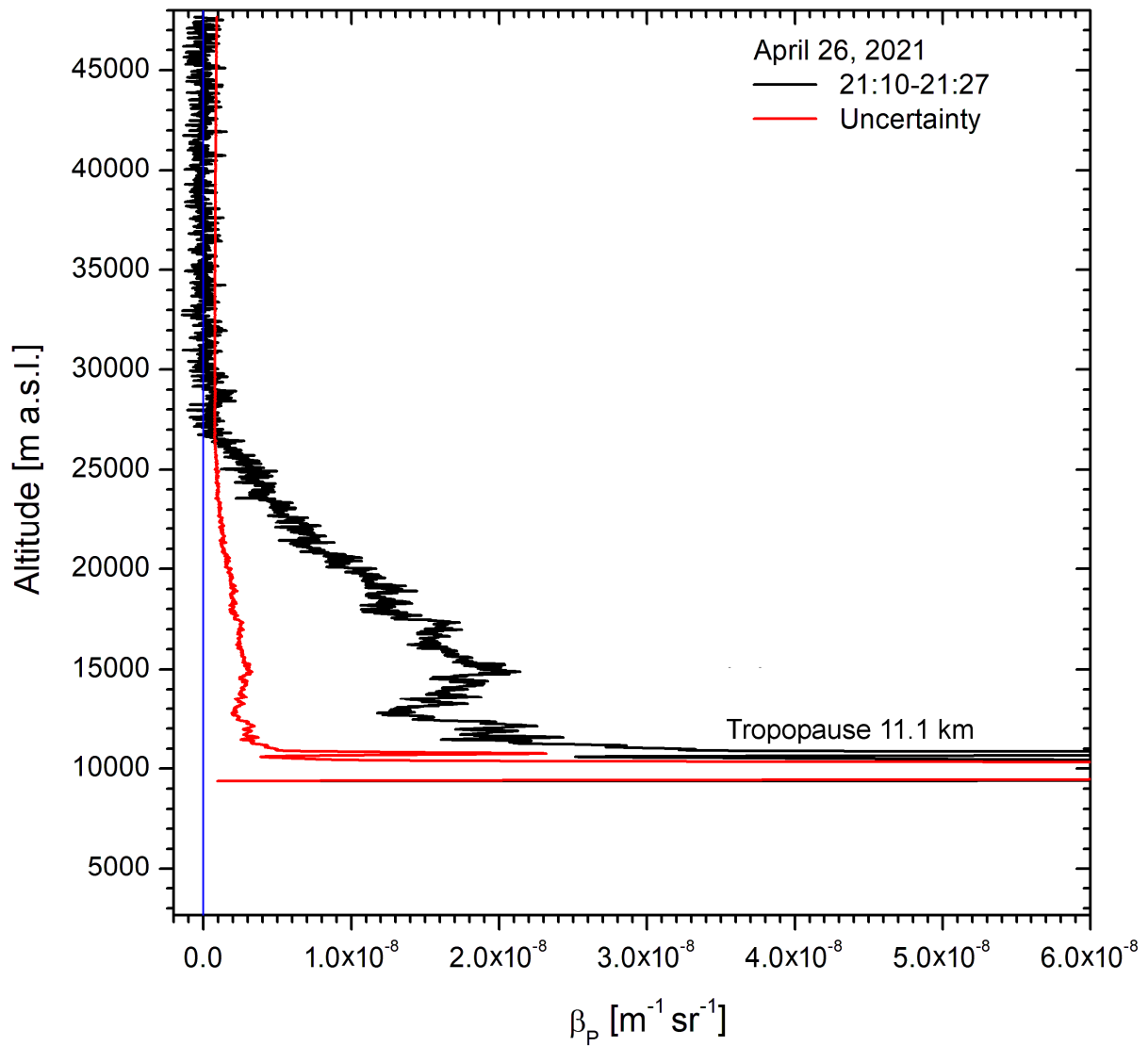
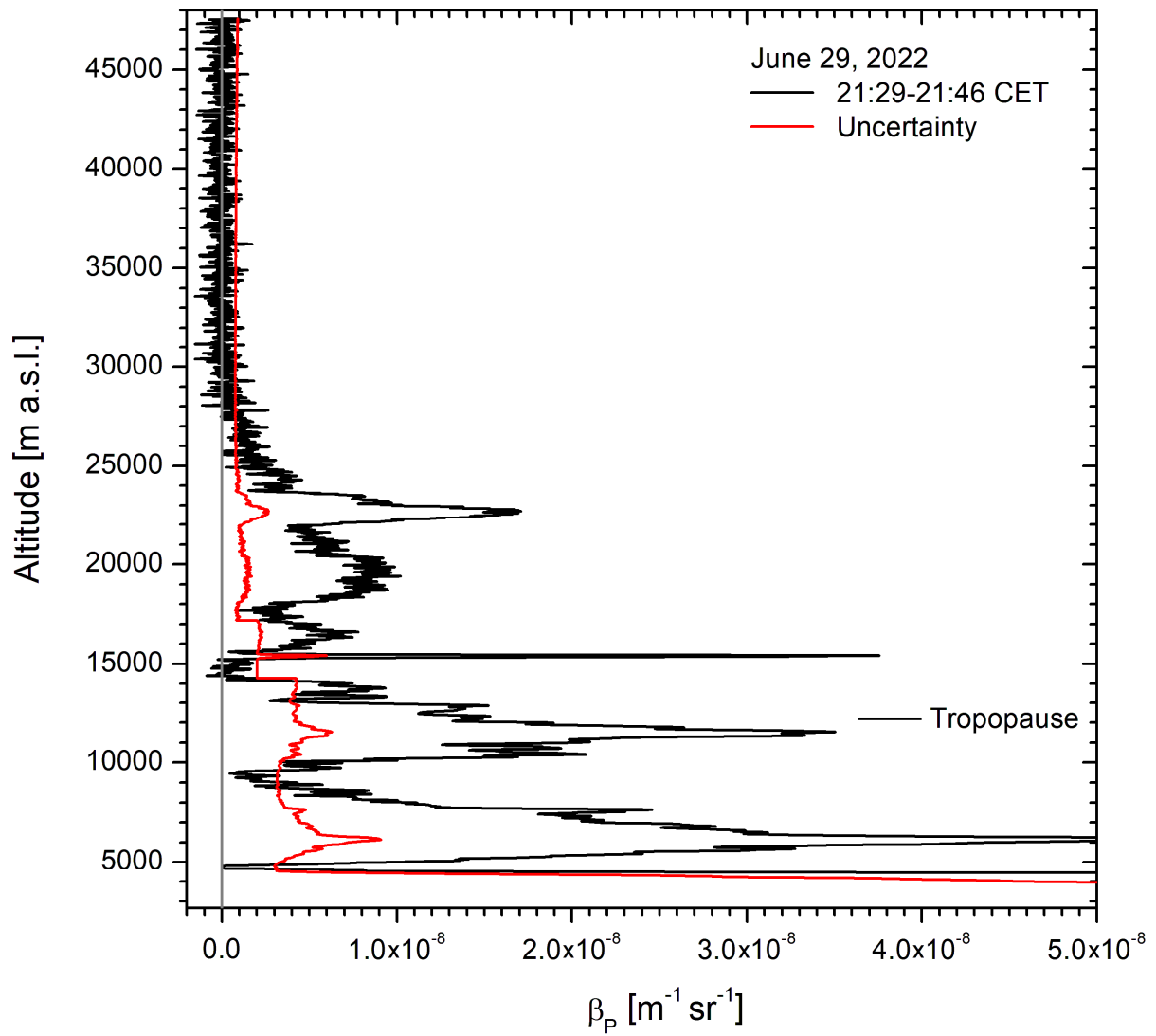


Fig. 12. Upper boundaries of the top aerosol layers after the two big volcanic eruptions in July 2019: “main layer” (blue) means more a pronounced aerosol feature already present before that period. We speculate that the rise of upper of the top boundary (red) was caused by northward propagation of the tropical eruption of Ulawun in the Brewer-Dobson circulation. The average scattering ratio (SCR) above 30 km is slightly elevated.

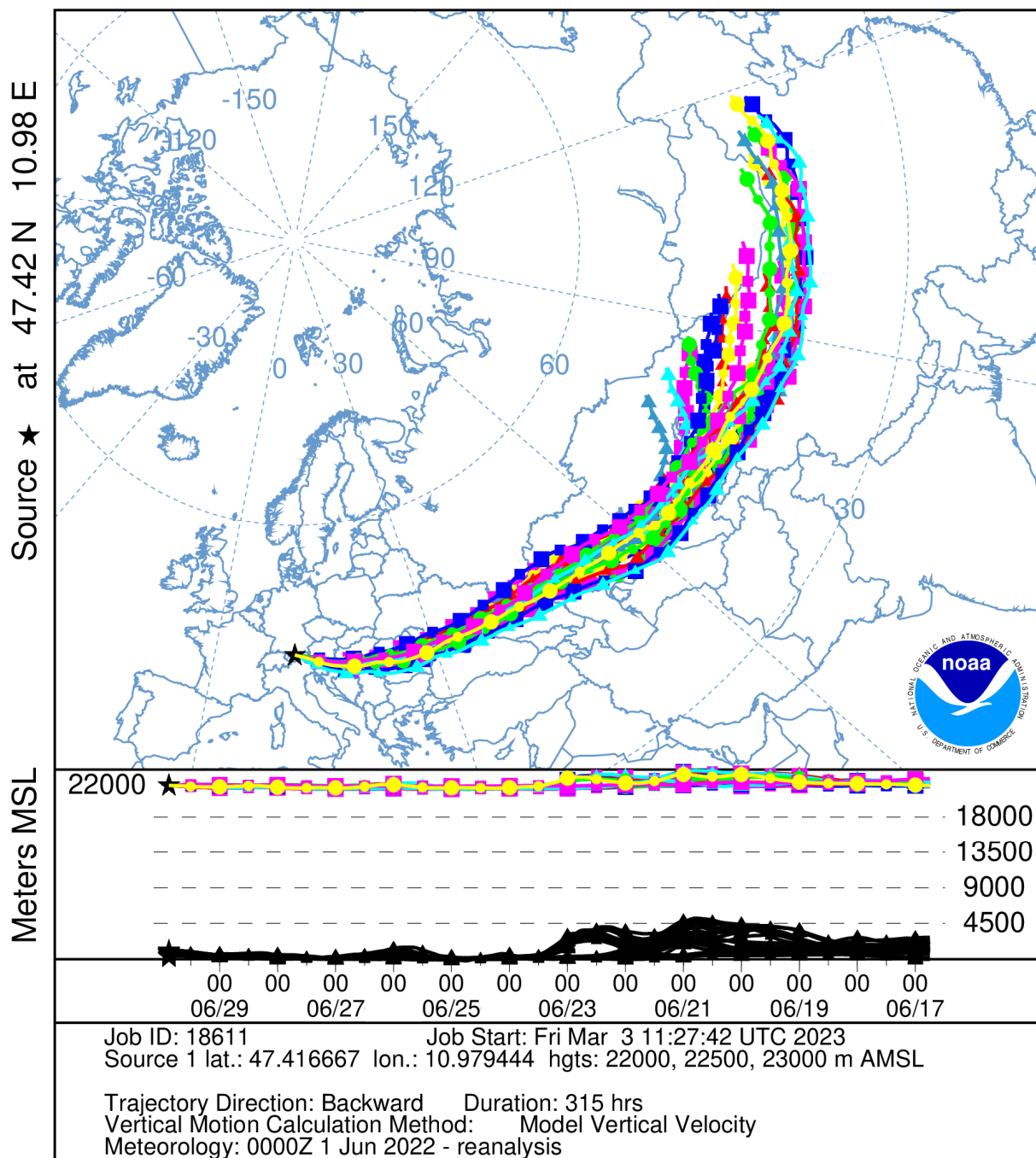


1245 **Fig. 13.** The 532-nm aerosol backscatter coefficients for 26 April 2021.: There are no longer aerosol contributions above 30 km. The strong cirrus signal did not allow a reasonable data evaluation within the troposphere.



1250 **Fig. 14.** 532-nm backscatter coefficients for the night-time measurement on 29 June 2022: The peak at 22.75 km is attributed to aerosol from the Hunga Tonga eruption on 16 January 2022 (see text). Please, note the rather low backscatter coefficients between 15 and 20 km that indicates the progress of aerosol removal from the stratosphere above our region after the recent events (see Fig. 12).

NOAA HYSPLIT MODEL
 Backward trajectories ending at 2100 UTC 29 Jun 22
 CDC1 Meteorological Data



1255 Fig. 15. HYSPLIT 315- h ensemble backward trajectories initiated above UFS on 29 June 2022 at 22:00 CET

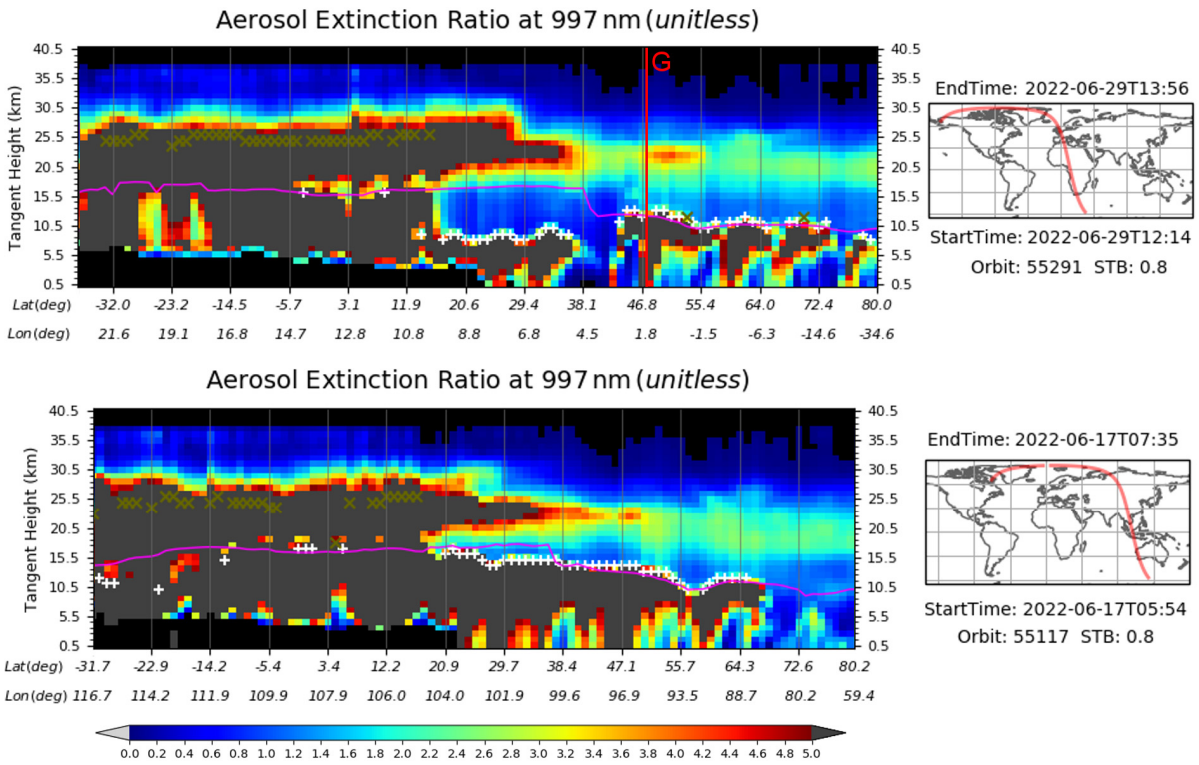
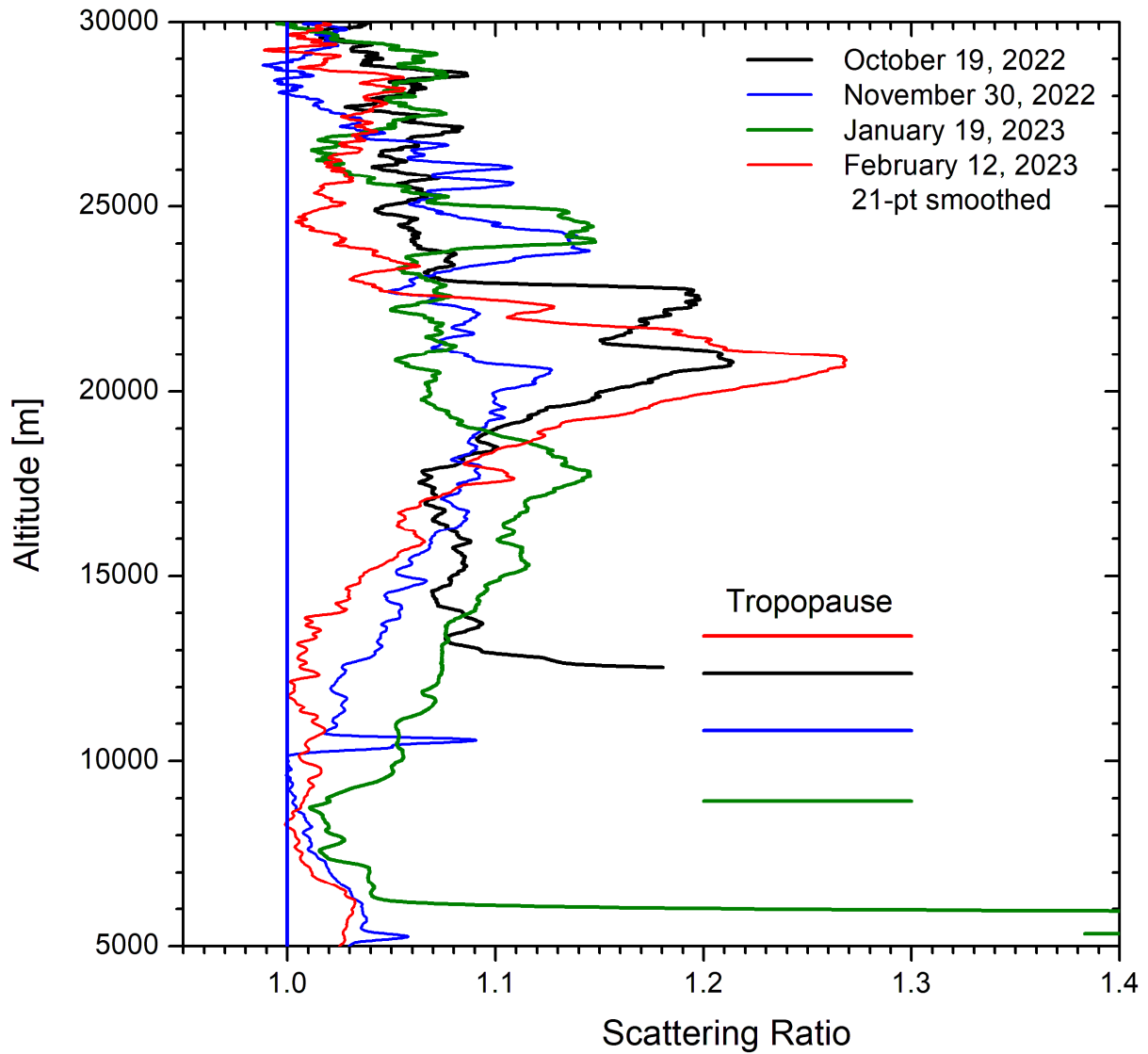


Fig. 16. OMPS vertical distribution of the 997-nm aerosol extinction ratio for orbits closest to UFS on 29 June (top) and over East Asia (bottom) on 17 June as indicated in Fig. 15; the vertical read line labelled by G marks the latitude of Garmisch-Partenkirchen. The panels to the right show the corresponding orbits of the satellite (red lines).

1260



1265 **Fig. 17.** Four selected profiles of aerosol scattering ratios between October 2022 and February 2023; the data are smoothed with ± 10 -bin gliding arithmetic averages. The tropopause altitudes are marked in the colours of the respective scattering ratios.

1270

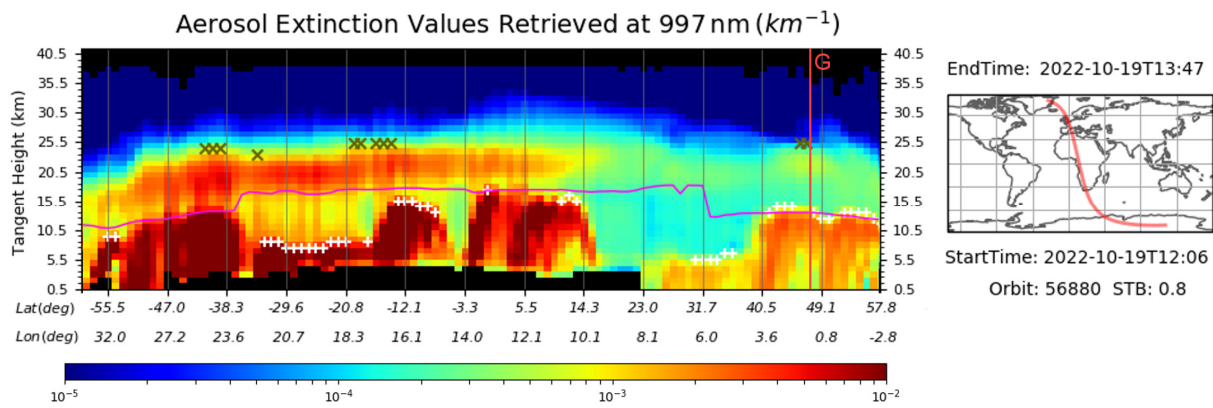


Fig. 18. Section of an OMPS curtain of the aerosol extinction coefficient along an orbit passing not far from Garmisch-Partenkirchen depicted in the right panel (19 October 2022); the elevated stratospheric aerosol caused by the Tonga eruption is located between roughly 56° S and 15° N, dark crosses marking pronounced aerosol layers. Slightly elevated aerosol is also seen around 47° N where also a few dark crosses are visible at 25 km.

1275

The violet line corresponds to the tropopause. The vertical red line visualizes the latitude of Garmisch-Partenkirchen (G).

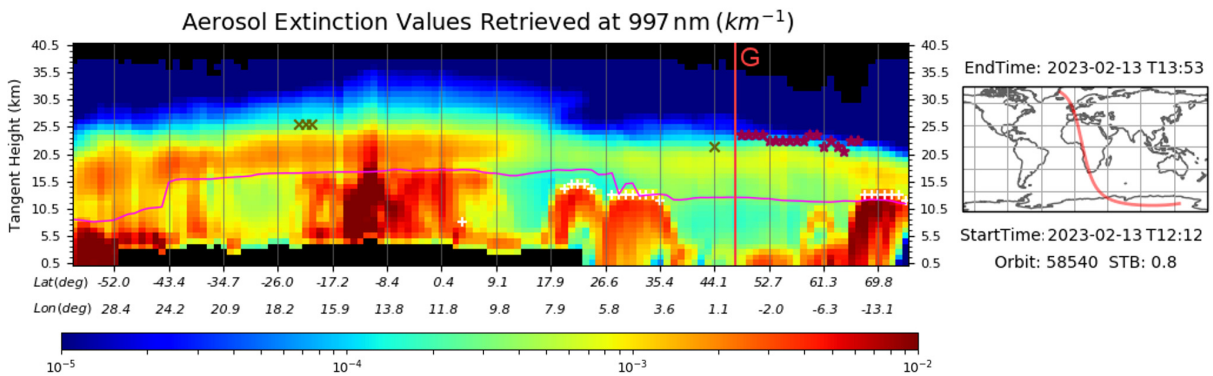


Fig. 19. Section of an OMPS curtain of the aerosol extinction coefficient along an orbit passing to the west of Garmisch-Partenkirchen depicted in the right panel (13 February 2023); dark crosses marking pronounced aerosol layers, red asterisks polar stratospheric clouds as determined by the OMPS algorithm. Slightly elevated aerosol is also seen around 47° N where also a few dark crosses are visible at 25 km. The violet line corresponds to the tropopause. The vertical red line visualizes the latitude of Garmisch-Partenkirchen (G).

1280